THESIS FOR THE DEGREE OF DOCTOR OF PHILOSOPHY

Supported Lipid Membranes and Their Use for the Characterization of Biological Nanoparticles

SILVER JÕEMETSA

CHALMERS

Department of Physics

CHALMERS UNIVERSITY OF TECHNOLOGY

Göteborg, Sweden 2020

Supported Lipid Membranes and Their Use for the Characterization of Biological Nanoparticles

SILVER JÕEMETSA

ISBN 978-91-7905-235-5

Doktorsavhandlingar vid Chalmers tekniska högskola, Ny series nr 4702

ISSN 0346-718X

Department of Physics
Chalmers University of Technology
SE-412 96 Gothenburg
Sweden
Telephone + 46 (0)31-772 1000

Printed at Chalmers Reproservice
Göteborg, Sweden 2020

Cover illustration: *Caricature of measuring a malicious but cute biological nanoparticle atop a supported membrane. (Margit Saal & Silver Jõemetsa)*

Supported Lipid Membranes and Their Use for the Characterization of Biological Nanoparticles

SILVER JÕEMETSA

Department of Physics

Chalmers University of Technology

Abstract

Biological nanoparticles (BNPs) are nano-sized lipid vesicles of biological origin, which are involved in multiple biological processes. BNP characterization techniques are critical for improving the understanding of how these particles contribute to cellular communication, viral infections and drug-delivery applications. However, due to their small size (between 50 and 200 nm in diameter) and molecular heterogeneity, quantitative characterization of their physical, chemical and biological properties is demanding, especially since their large structural and compositional heterogeneity calls for methods with single nanoparticle resolution. To address this challenge, work in this thesis has been focused on investigating and using supported lipid bilayers (SLBs) and their two-dimensional fluidity as a platform for nanoparticle characterization.

To investigate SLBs, we combined confocal microscopy with microfluidics to identify the mechanisms by which lipid vesicles are spontaneously converted into various types of planar membranes on a multitude of surfaces (Paper I) and found that most of the studied materials can support lipid film formation. In the context of SLB formation, specific focus was put on using total internal reflection fluorescence (TIRF) microscopy to monitor the kinetics of vesicle adsorption, rupture and spreading of individual SLB patches on glass (Paper II), revealing that the SLB formation process was driven by the autocatalytic growth and merger of multiple small SLB patches at appreciably high vesicle coverage. TIRF was also successfully employed to monitor lipid-enveloped drug permeation through an SLB formed on a mesoporous silica thin film (Paper III). The insights gained from investigating SLBs was also used for in depth characterization of BNPs using the surface-based flow-nanometry method, allowing for independent determination of size and fluorescence emission of individual BNPs tethered to a laterally fluid SLB formed on the floor of a microfluidic channel. This way we could demonstrate that the fluorescence emission from lipophilic dyes depends in a non-trivial way on nanoparticle size, and varies significantly between the different types of BNPs (Paper IV). The flow-nanometry concept was also used to elucidate the effect of vesicle size on their diffusivity on the SLB in the limit of few tethers (Paper V).

The insights gained in this thesis work on lipid self-assembly at different surfaces and the possibility to use SLBs on silica for in-depth characterization of BNPs demonstrate this as a promising approach in the field of single nanoparticle analytics, which in future work will be possible to extend into a novel means to probe interactions between BNPs and cell-membrane mimics representing a near-native situation.

Keywords: supported lipid bilayer, fluorescence microscopy, diffusion, size determination, lipophilic dyes, microfluidics

Appended Papers

Paper I

Molecular Lipid Films on Microengineering Materials
Silver Jõemetsa, Karolina Spustova, Kiryl Kustanovich, Alar Ainla, Severin Schindler, Siegfried Eigler, Tatsiana Lobovkina, Samuel Lara-Avila, Aldo Jesorka, and Irep Gözen
*Langmuir **2019** 35* (32), 10286-10298

Paper II

Spatiotemporal Kinetics of Supported Lipid Bilayer Formation on Glass via Vesicle Adsorption and Rupture
Mokhtar Mapar, Silver Jõemetsa, Hudson Pace, Vladimir P. Zhdanov, Björn Agnarsson, and Fredrik Höök
The Journal of Physical Chemistry Letters **2018** 9 (17), 5143-5149

Paper III

Investigating Poorly Water-Soluble Drug Permeation Across a Lipid Membrane Supported on Mesoporous Silica
Paul Joyce, Silver Jõemetsa, Simon Isaksson, and Fredrik Höök
Submitted

Paper IV

Independent Determination of Size and Fluorescence Emission of Individual Biological Nanoparticles Reveals that Incorporation of Lipophilic Dyes Does Not Correlate with Particle Size
Silver Jõemetsa, Paul Joyce, Quentin Lubart, Mokhtar Mapar, Emanuele Celauro, Björn Agnarsson, Stephan Block, Marta Bally, Elin Esbjörner Winters, Gavin D.M. Jeffries, and Fredrik Höök
Submitted

Paper V

Effects of Vesicle Size on Their Diffusivity when Linked to a Supported Lipid Bilayer
Silver Jõemetsa, Erik Olsén, Adrián González Rodríguez, Paul Joyce, and Fredrik Höök
In manuscript

Contribution Report

Paper I

I planned, guided and performed the major part of the experiments and associated data analysis. I contributed significantly to the writing of the manuscript.

Paper II

I planned and performed part of the experiments. I was extensively involved in the data analysis and the writing of the paper.

Paper III

I planned and performed part of the TIRF experiments. I was extensively involved in the data analysis and writing process.

Paper IV

I planned and performed all the flow nanometry experiments, including microfluidics designs. I analyzed the data and wrote the main part of the manuscript.

Paper V

I planned and performed most of the flow nanometry experiments, analyzed the data, and wrote the main part of the manuscript.

Abbreviations

2DFN	two-dimensional (2D) flow nanometry
AD	Alzheimer's disease
AFM	atomic force microscopy
ATTO488PE	1,2-Dipalmitoyl-sn-glycero-3-phosphoethanolamine labeled with Atto 488
BNP	biological nanoparticle
C8	caprylic acid
CLSM	confocal laser scanning microscopy
cryoEM	cryo-electron microscopy
DLS	dynamic light scattering
DOPE	1,2-dioleoyl-sn-glycero-3-phosphoethanolamine
DOTAP	1,2-dioleoyl-3-trimethylammonium-propane
EM	electron microscopy
EV	extracellular vesicle
FaSSIF	fasted-state simulated intestinal fluid
FCM	flow cytometry
FRAP	fluorescence recovery after photobleaching
HSV-1	Herpes Simplex type 1 virus
iSCAT	interferometric scattering microscopy
MSD	mean squared displacement
MSN	mesoporous silica nanoparticle
MSTF	mesoporous silica thin film
NMV	native membrane vesicle
NTA	nanoparticle tracking analysis
PDMS	poly-(dimethylsiloxane)
POPC	1-palmitoyl-2-oleoyl-sn-glycero-3-phosphocholine
RPS	resistive pulse sensing
SLB	supported lipid bilayer
spDIO	3,3'-Dioctadecyl-5,5'-Di(4-Sulfophenyl)Oxacarbocyanine
SUV	small unilamellar vesicle
TEOS	tetraethyl orthosilicate
TIRF	total internal reflection fluorescence

Table of Contents

Introduction

"The oldest and strongest emotion of mankind is fear, and the oldest and strongest kind of fear is fear of the unknown." – H. P. Lovecraft

Life is a complex interplay between various physical and chemical processes that are integral to maintaining life, facilitating growth and preventing disease. Debilitating and fatal diseases that exist without a cure threaten this balance and consequently our well-being, be it cancer, viral infections or neurodegenerative disorders, such as Alzheimer's disease (AD). As an instructive illustration, it is worth considering AD as an increasingly common, fatal and incurable neurodegenerative disorder that impairs the memory and intellectual functioning of about 50 million people worldwide [1]. Current treatment methods are capable of suppressing symptoms and slowing the progression of the disease, but for such techniques to be effective, early identification and diagnosis is paramount. Since the largest personal suffering, both for the patient and family, as well as cost for AD comes from continued patient support and care, once the disease has already progressed, there is an urgent need to develop new technologies that can detect the disease prior to symptoms being prevalent.

One of the common factors involved in AD and many other incurable conditions are small, nano-sized objects of biological origin, called biological nanoparticles (BNPs). Many of these particles are enveloped by a lipid membrane, thus sharing similarities with the host cell's plasma membrane. This membrane, containing various phospholipids, proteins and carbohydrates, protects the internal content from the external environment. BNPs are responsible for a multitude of processes in the body, ranging from the aforementioned pathological conditions [2] to intercellular communication that maintain health [3]. Furthermore, these particles have been proven to be natural and effective carriers of bioactive molecules, such as miRNA, mRNA, DNA, lipids, and proteins. This combination of biocompatible envelope and their ability to carry bioactive cargo makes them an attractive target and serves as inspiration for drug delivery carriers. It has therefore been hypothesized that improved nanoparticle analysis techniques should contribute to better diagnosis [4] while simultaneously enhancing the understanding of the pathogenic and functional role of BNPs [5] as well as their potential use as drug delivery carriers or inspiration for the same [6,7].

Extracellular vesicles (EVs) are one example of BNPs, being excreted from every cell type into body fluids such as plasma, urine and saliva [8]. They are highly heterogeneous and believed to be involved in the progression and infection steps of a multitude of diseases, such as cancer [9] and different neurological conditions [2,8]. For instance, EVs are suggested to be involved in transferring proteins associated with AD between cells, thus causing accumulation and aggregation of proteins in otherwise healthy cells [2]. There are also recent findings suggesting that various viruses are transmitted as viral cargo inside EVs [10,11]. Consequently, their abundance and involvement in various biological processes makes EVs relevant as diagnostic biomarkers. In order to gain insight into how they contribute to the development of diseases, as well as cellular functions, it is of relevance to investigate their huge compositional heterogeneity, which would enable their future use as both diagnostic biomarkers and novel therapeutic delivery vehicles. However, the combination of nano-scale size (typically 50 to 200 nm in diameter) and high molecular heterogeneity makes the characterization of these nanoparticles challenging [12].

This thesis work puts focus on gaining fundamental knowledge of the properties of BNPs and their interactions with model cell membranes. In order to first characterize how different biologically relevant materials interface with lipid membranes, for potential biophysical as well as biomedical applications such as implants and drug-delivery, we combined confocal laser scanning microscopy (CLSM) with an open-volume microfluidic device, to deliver lipid vesicles onto a multitude of biologically relevant planar surfaces to identify the mechanism by which the membranes interfaced with the material and the fluidic properties of the membrane assemblies (Paper I). A specific objective was to gain insight about the supported lipid bilayer (SLB) formation on borosilicate glass, by which total internal reflection fluorescence (TIRF) microscopy was used to monitor the kinetics of vesicle adsorption and subsequent rupture into individual SLB patches on borosilicate glass (Paper II). Once SLB formation was successfully characterized on various surfaces, we were interested in monitoring lipid-enveloped drug permeation across an SLB formed on a mesoporous silica thin film, by confining the TIRF evanescent wave within the pores of the thin film (Paper III).

For the purpose of characterizing the heterogeneity of BNPs, a newly developed tool for the characterization of individual nanoparticles was utilized, enabling simultaneous determination of size and molecular content [13] on the level of individual BNPs by propelling them using a hydrodynamic force after being tethered to a mobile SLB. One key aim of this work was to elucidate how the incorporation efficiency of dyes depends on the size of BNPs

by independently measuring size and fluorescence emission of self-inserting dyes (Paper IV). More specifically, by comparing synthetic lipid vesicles, native-membrane vesicles and EVs, the approach was utilized to investigate how the incorporation efficiency of a commonly used membrane-staining dye depends on BNP size and membrane properties. This size determination tool was also employed to differentiate between vesicle populations tethered to the SLB with different number of linker molecules and to disentangle the effect of vesicle size on their diffusivity from the diffusivity of the linker itself (Paper V).

The objective of this thesis is to provide the foundation for the experimental and analytical work leading up to the results presented in the appended papers. Specifically, to familiarize the reader with the biologically relevant concepts, Chapter 1 presents in further detail lipid vesicles, supported lipid membranes, their interactions with surfaces and BNPs. Chapter 2 gives an overview of the most commonly used single-nanoparticle characterization tools for BNPs; listing their unique strengths and limitations with an emphasis on size and molecular content determination. Chapter 3 includes the principles for the methods used in this research with an emphasis on two-dimensional flow nanometry. Chapter 4 summarizes and discusses the results of the appended papers. Finally, Chapter 5 concludes this thesis with an outlook for future research plans towards an even greater BNP characterization toolbox.

1 Biological background

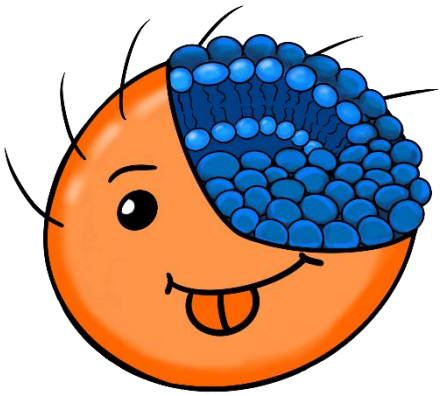

The cells in our bodies are amazingly complicated autonomous units of life, which contain many biomolecules that serve as the building blocks of our bodies – e.g., proteins and lipids. Similarly, to how proteins assemble into higher ordered structures, so do the lipids which comprise the protective layer around cells. This chapter will be insightful to those who are interested in what lipids are and the various ordered structures they spontaneously form into.

1.1 Phospholipids and self-assembly

Lipids are amphiphilic molecules that are characterized by a unique molecular structure comprised of a hydrophilic (polar) head-group attached to hydrophobic (non-polar) alkyl chains or 'tail-groups' [14]. Lipids are essential to all forms of life and the functional properties of each are controlled by the chemical nature of their head-group and the length, number and saturation of the tail groups [15].

Of significant interest are phospholipids (phosphoglycerides), which are the main constituents of biological cell membranes and are, thus, essential for regulating cellular processes, function and health [16,17]. The plasma membrane constitutes a two-dimensional medium made up of a fluidic phospholipid bilayer that is host to a multitude of biological macromolecules, such as transmembrane proteins and carbohydrates. Owing to its unique structure, the cell membrane acts as a protective vessel for cell organelles separating the intracellular and extracellular spaces, while its semi-permeable properties facilitate transport of specific nutrients and waste products into and out of the cell [18]. The latter function, which is crucial for cellular communication, depends critically on key proteins and lipids that are embedded within the phospholipid bilayer.

Phospholipids are structurally comprised of two fatty acid groups linked to a glyceryl backbone [19]. Unlike other lipids such as triglycerides, the third glycerol hydroxyl group is replaced with a phosphate head-group, rather than a fatty acid chain (Figure 1). In biological

membranes, hydrocarbon tails typically contain 10 to 18 carbons per chain, which are linked together by single bonds (saturated) or double bonds (unsaturated).

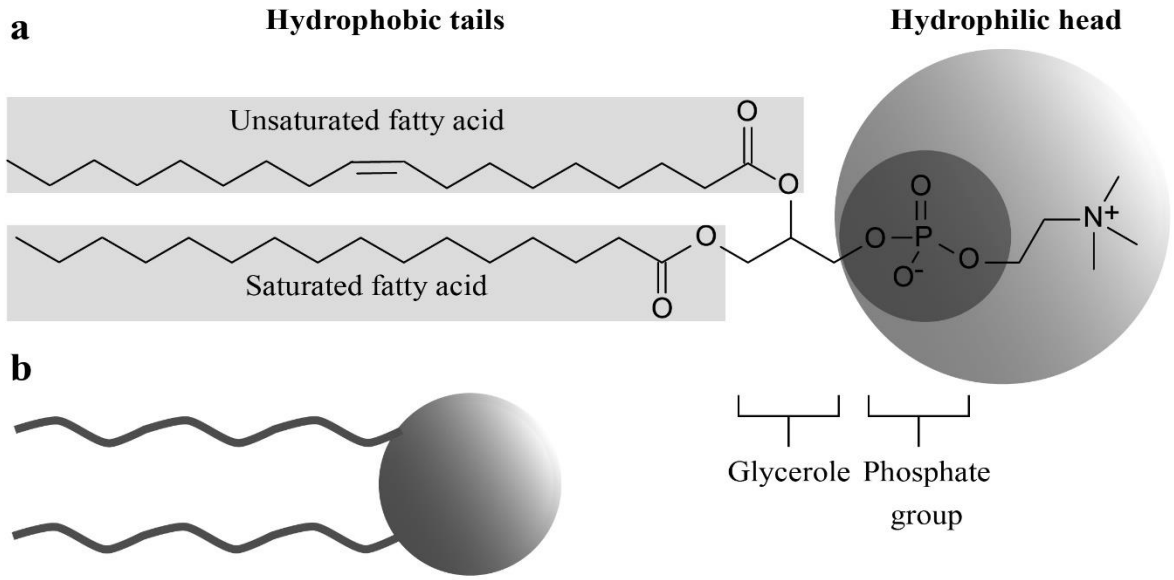

Figure 1. (a) Schematic representation of the phospholipid molecule 1-palmitoyl-2-oleoyl-glycero-3-phosphocholine (POPC) depicting the polar head-group, non-polar tail-groups, fatty acid chain saturation and additional chemical units. (b) A simplified illustration of a phospholipid.

In the process of minimizing the free energy, the hydrophilic head of lipids screen the hydrophobic tails by spontaneously forming aggregates when dispersed in an aqueous solution, which is often referred to as the 'hydrophobic effect' [20]. The spontaneous organization process of lipids (and other amphiphiles) from a disordered state to an ordered or semi-ordered arrangement is a thermodynamically driven process referred to as molecular self-assembly. Exposure of water molecules to the non-polar component of lipid molecules contributes to a reduction in H-bonding between water molecules [21]. If the hydrophobic molecule is small, water molecules salvage the lost H-bonds by forming cages that envelope the molecule with minimal termination of these bonds, known as hydrophobic solvation. However, the interaction between water molecules near a larger hydrophobic interface is highly thermodynamically unfavorable, because the newly formed configurations have an increased degree of order, which in turn corresponds to a reduction in entropy. All closed systems strive towards increasing the entropy and thereby contributing to minimizing the Gibbs free energy (ΔG) of the system, given by:

$$\Delta G = \Delta H - T\Delta S\,, \qquad 1.1.1$$

where ΔH is the change in enthalpy, ΔS is the change in entropy and T the temperature. It should be noted that for a spontaneous process, such as molecular self-assembly, to occur, the change in free energy must be $\Delta G < 0$. Despite the self-assembly of lipid molecules into an organized lipid membrane contributing to a lowering of the entropy, the overall entropy of the lipid-containing aqueous solution increases ($\Delta S > 0$) due to release of ordered water around the hydrophobic tails, and accordingly the free energy is reduced. It should also be noted that in the case of lipid self-assembly in aqueous solutions, the change in enthalpy (ΔH) is negligible compared to the $T\Delta S$ term [22], which means that it is an entropy driven process. This is a biological design principle that goes beyond lipid molecules, and although the enthalpic contribution is often appreciable, spontaneously self-assemble into various organized structures in aqueous media can often be viewed as a tendency to 'hide' their hydrophobic regions from water.

Different lipid molecules can form colloidal structures of various types and geometries. These are determined by the effective head-group area, critical chain-length and hydrocarbon volume of the lipids [15]. This can be stipulated by relating the shape of the amphiphile to the critical packing parameter (CPP):

$$CPP = \frac{V}{AL}, \qquad 1.1.2$$

where V is the volume taken by the hydrophobic (tail) part, A is the effective surface area of the head-group and L is the length of the tail-group. Single-chained lipids with bulky head-groups, defined by $CPP < 1/3$, such as the common detergent sodium dodecyl sulfate (SDS), tend to form spherical micelles; single-chained lipids with small head-groups, defined by $1/3 < CPP < 0.5$ tend to form cylindrical micelles; phospholipids with two tails and a fairly large head-group, defined by $0.5 < CPP < 1$ tend to form bilayers and vesicles; and lipids with large hydrophobic tails, defined by $CPP > 1$, prefer to form reverse phases, such as inverted micelles [22]. Most phospholipids have a cylindrical shape, i.e., $CPP \sim 1$, and therefore tend to form lipid bilayer structures. However, the CPP of the self-assembled lipid-based structure depends on numerous parameters, such as electrolyte composition and water to lipid ratio, pH, and temperature, as these factors influence the interactions between the lipid aggregates and also the intermolecular forces within each aggregate.

One of the most attractive lipid-based structures used extensively in biophysical investigations of cell-membrane properties are vesicles or liposomes, which are spherical

compartments defined by an outer lipid bilayer structure. In living organisms, vesicles are either naturally occurring, originating from the cell, such as extracellular vesicles and exosomes [23] or they may be artificially created from preselected lipid components. Specifically, they can be produced directly from cell membranes, such as the native membrane vesicles used in this thesis work, isolated from cells [4] or artificially made from dissolved lipids [24]. Vesicles are typically classified according to their size and number of bilayers. That is, vesicles may be classified as small (10-100 nm), large (100-1000 nm) and giant vesicles (larger than 1 μm), and as either uni- or multi-lamellar. The hydrophobic interior of lipid bilayers is a relatively homogeneous region of hydrocarbon chains, whereas the exterior is comprised of the hydrophilic head-groups, which orient towards the aqueous medium [22,25]. Due to the simplicity by which they can be produced, intrinsic biocompatibility and biodegradability, vesicles have been used extensively in the food industry. They are also employed as nanocarriers in drug-delivery applications thanks to their high stability and life-time, and as biophysical models to probe different cell-to-cell interactions [26]. Different types of vesicles are also used as simplified model systems for cell membranes, and are in fact the key component in most artificial cell systems [27–30].

1.2 Lipid-surface interactions

The structure and orientation of lipid assemblies on inorganic surfaces are dependent on fundamental properties associated with the underlying solid surface, such as surface chemistry and roughness. Accordingly, it is critical to know the properties of the surfaces in question, in order to control the propagation of lipid molecules. One of the fundamental properties of surfaces is their excess energy, due to unsatisfied coordination of the surface molecules. Since all systems strive to minimize their free energy, surface atoms tend to decrease this excess energy by forming new bonds with molecules in their vicinity. This difference in energy between the atoms on the surface and in the bulk is called the surface free energy ($\mathcal{F}$) which is a measure of how much work is necessary to form a unit area of surface [31]. In the case of a solid material, the creation of this area can be visualized by cleaving a block of material into two pieces, which will result in the breakage of chemical bonds. During this process the number of atoms will not change, only the surface area of the material.

The surface tension of a material (γ) is determined by the surface free energy ($\mathcal{F}$) and is represented as the tangential stress (force per unit length) in the surface layer [32]:

$$\gamma = \mathcal{F} + A\frac{\partial \mathcal{F}}{\partial A}, \qquad 1.2.3$$

where A is the area of the surface and the derivate $\partial\mathcal{F}/\partial A$ describes the induced bulk stress in a solid after deformation (elastic strain changing the surface density of atoms). Solid materials cannot balance this stress since their atoms are immobile thus preserving their relative positions after deformation. In case of one-component liquids, since the molecules can move freely between the surface and the interior during deformation, $\partial\mathcal{F}/\partial A = 0$, hence $\gamma = \mathcal{F}$ [33].

Based on the strength of the bonds holding a material together, it is possible to predict the tendencies to be wetted by liquids. Materials with high energy bonds such as covalent, ionic and metallic are considered high-energy surfaces, whereas low-energy surfaces are often polymers with covalently bonded chains that are held together by weak intermolecular van der Waals forces. It is common to categorize surfaces based on their interactions with water only. They can be hydrophilic (polar) i.e., water-friendly or hydrophobic (non-polar) i.e., water-fearing. For hydrophilic high-energy surfaces, the energy of the system is minimized by increasing the contact area between the lipid and surface. However, the reason why lipid monolayer adsorption and spreading occurs on hydrophobic low energy substrates is because the hydrophobic tails of the lipid shield the surface from water [34].

Since many lipid molecules are charged, the charge on the surface can affect lipid-surface interactions as well. In principle, all surfaces in contact with a liquid of a high dielectric constant, such as water, carry a surface charge [22]. The charge can either originate from the ionization or dissociation of surface groups or by the association of ions from solution onto previously uncharged surfaces [22,35]. For chemically inert materials such as Teflon AF, the preferential adsorption of hydroxyl ions due to the orientation of water at the hydrophobic interface appears to be the reason [35,36]. The surface charge on oxides results from the ionization of the previously formed hydroxyl groups on the surface upon contact with water [37]. The charge on a surface can be negative, positive or zero, depending on the nature of the oxide in question and the pH of the surrounding buffer. Nonetheless, in such a solution, the charge on the surface is balanced by a thin stationary layer of oppositely charged but equal counterions (called the Stern layer). These ions originate from the so-called diffuse layer in close proximity of the surface, where rapid thermal motion between both counter- and co-ions

occurs. The charge on a surface can thus be assessed by the zeta potential at the slip surface within the diffuse layer [38]. These properties affect lipid propagation/spreading on surfaces among others, such as the roughness of the surface [39].

1.3 Supported cell-membrane mimics

In order to gain insights into cellular processes and activities that are fundamental for cell survival, considerable focus in recent decades has been directed towards analyzing the molecular interactions with and between lipid bilayer membranes. One attractive approach to investigate key biophysical features of biological cell membranes that meets the requirements of many high-end analytical tools is to make use of the property that vesicles can be converted to various membrane assemblies when interacting with solid surfaces. Indeed, a large variety of different lipid structures can be formed on solid interfaces [40,41], including single bilayers [42], double bilayers [39,43] or monolayer lipid films [44,45], which can be controlled by the preparation technique, the lipid composition and charge, the ionic strength of the surrounding solution and the properties of the support surface. Considering the aforementioned complex lipid-surface interactions, it is non-obvious what type of pathway, e.g., adhesion, rupture and/or spreading, the vesicles will follow. Supported membranes are typically formed on borosilicate glass, silica and atomically smooth mica [46–48]. However, since other biologically relevant surfaces offer various benefits, studying the membrane formation and integrity on these surfaces is of practical and scientific relevance. The formation of membranes on inorganic solids and polymers allows for biological functionalization [49]. Thus, a better understanding of the lipid-surface interactions can potentially increase biocompatibility of implant materials, such as aluminum oxides [50] and TiO_2 [51] even further. Another application of interest is the design of biosensors based on supported membranes, where sensing is based on the signal of conductive materials, such as Au, graphene [52,53] and ITO [54,55]. SiC combines these two applications by being a potential in-vitro biosensor due to its sensing capabilities and biocompatibility [56,57]. All of these materials are optically transparent and therefore compatible with microscopy approaches. In Paper I, the interactions between lipids and the aforementioned surfaces were investigated.

One particularly attractive cell membrane mimic of this type is the so-called supported lipid bilayer (SLB), which exists as a planar surface confined lipid membrane that retains two-dimensional fluidity, while providing reduced complexity and greater stability for the lipid membrane compared with cell membranes. The 2D fluidity of SLBs is believed to be maintained by a 1–2 nm layer of trapped water between the substrate and the bilayer [58–60].

When combined with the compatibility of arbitrary sized planar surfaces, SLB fluidity is the prime reason for their functionality and efficacy in providing detailed insights into cellular membranes, when applied in combination with sensitive analytical techniques e.g., atomic force microscopy [61], fluorescence microscopy [62], quartz crystal microbalance, surface plasmon resonance [63] among others [64]. However, owing to the reduced complexity, it is crucial to carefully characterize these native membrane mimics as accurately as possible to represent the appropriate membrane function for a given application. Thus, significant efforts have been invested into the characterization of the formation mechanism under various conditions [34,40,46,48,65,66]. In this work, we contributed to this tradition by investigating the SLB formation process on borosilicate glass, which was investigated in both Papers I and II.

In addition to SLBs, other types of biologically relevant membranes can be assembled depending on the surface. In contrast to SLBs which require hydrophilic supports, lipid monolayers assemble on hydrophobic low-energy surfaces such as certain photoresists and fluorinated polymers e.g., SU8, or Teflon AF, where the hydrophobic tails of the single layered lipid film are arranged towards the substrate [34]. Albeit the use of lipid monolayers as cell membrane models is limited due to their inability to incorporate transmembrane proteins and other components which are essential for many biophysical studies, they are found in biological systems, such as the lung surfactant in the alveoli [67,68] or the protective tear film on the corneal epithelium of the eye [69,70]. Due to their structural simplicity, they are also used as biomimetic coatings, for example in research towards novel targeting approaches to aid in the diagnosis of Alzheimer's disease and dementia [71,72]. An alternative pathway compared to SLB formation on high-energy hydrophilic surfaces is the formation of double bilayer membranes, which are essentially surface-adhered giant unilamellar vesicles with a minimal encapsulated volume [39,43]. Small unilamellar vesicle (Figure 2a) adsorption and their rupture into various supported membranes upon contact with a favorable surface were systematically investigated in Paper I on different optically transparent microengineering materials.

As a general rule, if the surface is hydrophilic, a single bilayer [42] or a double bilayer [39,43] is formed, while hydrophobic surfaces lead to monolayer lipid films [44,45] (Figure 2b-d). Of particular interest are SLBs, which have a typical thickness of 4 to 5 nanometers (Figure 2b). In order to form SLBs with low defect density and high mobility, the surface should be hydrophilic, smooth and clean [73].

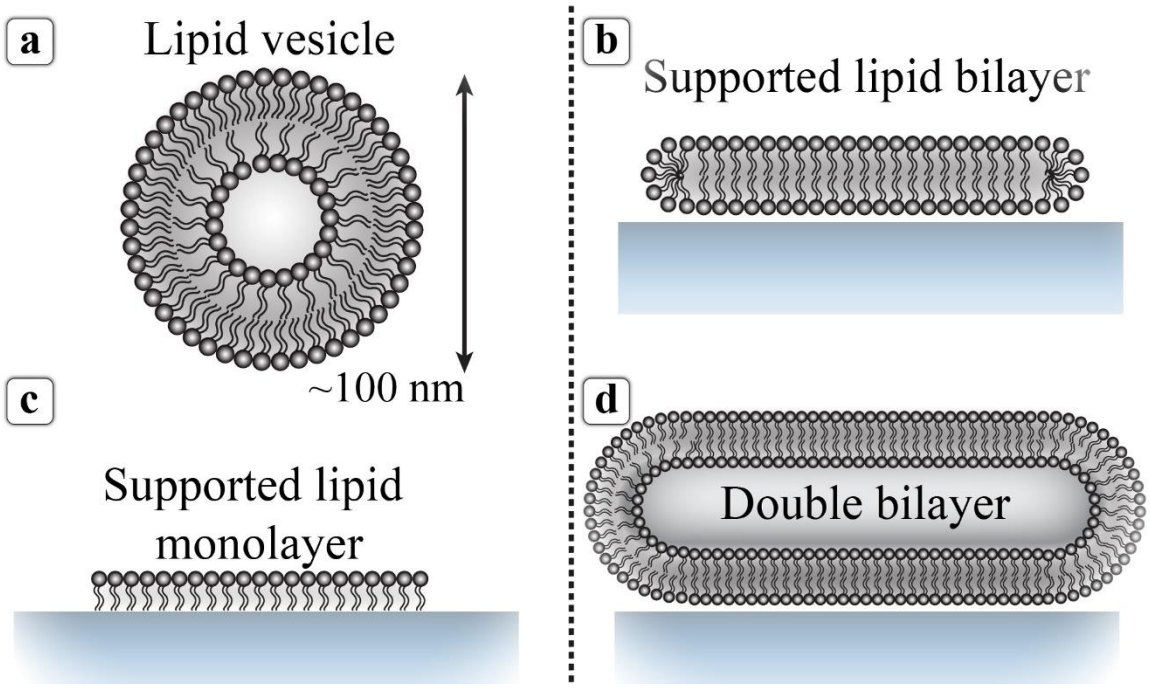

Figure 2. The cross-section of a vesicle (a). Various supported membranes: (b) a supported lipid bilayer, (c) supported lipid monolayer, and (d) double bilayer.

The historically predominant methods for surface deposition of lipid bilayers were Langmuir–Blodgett (LB) and Langmuir-Schaefer (LS) [34,74], with which multiple lipid monolayers are transferred onto planar surfaces as they are successively transferred up and down across a liquid-air interface containing a lipid monolayer, while more recent methods include solvent-assisted lipid deposition [75] and a method where freeze-thawing is used to induce vesicle rupture and subsequent membrane formation [76]. The most popular membrane formation method, which was also used in this thesis work, is the adsorption and fusion of vesicles [77,78]. In this case, vesicles approach the surface via diffusion from the bulk and adsorb if the surface-vesicle interaction is favorable. Although vesicles can occasionally rupture into small bilayer patches at a relatively low vesicle coverage, the SLB formation is initiated when a fairly high vesicle coverage is reached, after which they start to rupture into small patches that initiate growth and the auto-catalytic SLB formation cascade [63]. In Paper II, the aforementioned observations were investigated in detail by following the growth kinetics of individual SLB patches from the adsorption and rupture of vesicles on glass.

Not only does the type of formed membrane depend on the surface, but the properties of the lipids themselves can be affected, such as their diffusivity. Planar silica and glass have been used extensively, therefore it is of interest to see how the porosity of the substrate reduces contact points with the membrane and consequently increases diffusivity of the lipids within

the SLB, thus we used mesoporous silica thin films (MSTF). MSTF are excellent interfaces for biomedical applications such as drug-delivery due to their tunable pore size and high biocompatibility [79]. The honeycomb-like porous structure enables the encapsulation of high concentrations of bioactive molecules such as proteins, retaining their function in the silica matrix [80,81]. MSTF have also been used as supports for SLBs enabling the incorporation of transmembrane proteins [82]. The diameter of pores in the mesoporous range are 2-50 nm by definition [83] and can be tuned by altering the soft templating agent, which is commonly either a surfactant [84] or block copolymer [85]. In Paper III, we monitored poorly water-soluble drug permeation through SLBs formed on MSTFs. These MSTFs were formed using a sol-gel process [86], in which the hydrolysis of the silica precursor tetraethyl orthosilicate (TEOS) was followed by the condensation into an amorphous silica network around a polymer template. The silica precursor solution was deposited on a glass surface via spin-coating. Later the templating polymer was burnt off to leave a thin film of mesoporous silica with an average pore size of 7 nm (Figure 3). The formed silica surface was treated with UV-ozone to promote the exposure of hydrophilic hydroxyl groups and carried a net negative charge at physiological pH.

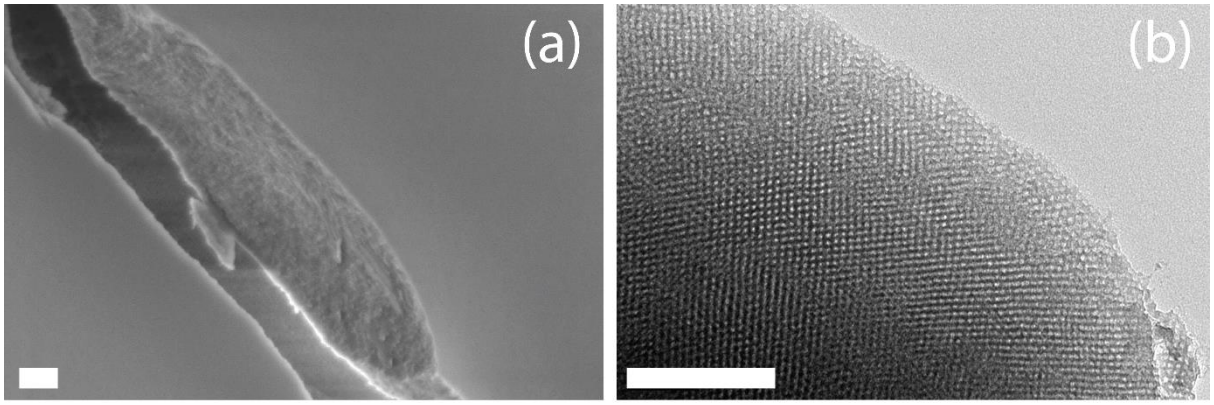

Figure 3. (a) Scanning electron and (b) transmission electron micrographs of MSTF. Scale bars are 200 nm.

SLBs are also attractive environments for the incorporation of biological molecules which function within the membrane, such as transmembrane proteins, or bind to the membrane, as covered in numerous review articles [21,49,60,87]. More artificial molecular constructs can also be attached to SLBs, where they can serve as linker molecules. The most popular example is the high-affinity binding between biotin and streptavidin [88]. Our group pioneered the use of membrane self-inserting cholesterol-DNA [89,90] to anchor and investigate the mobility of tethered nanoparticles [91]. This approach was used in Paper IV, which was focused on

studying the self-insertion of lipophilic dyes into various biological nanoparticles and in Paper V to study the properties of the actual linker itself.

1.4 Biological nanoparticles

Biological nanoparticles (BNPs), such as extracellular vesicles, exosomes and viruses are involved in a multitude of functional as well as pathogenic biological processes, including cellular communication and viral infection; the detailed molecular mechanisms of which are not yet fully understood. Accordingly, the characterization of BNPs and their associated processes has emerged as a focus area for the improved understanding of fundamental processes that control cellular health. Furthermore, many BNPs have been proven to be efficient carriers of various bioactive molecules, such as mRNA, DNA and proteins within their membrane envelope. Therefore, insights derived from investigations directed towards BNPs can be harnessed for biomimetic development of novel therapeutic delivery vehicles.

1.4.1 Viruses

Viruses are complex molecular machines capable of infecting allegedly all cellular life. Virus particles vary considerably in size and shape, ranging from 20 nm to 500 nm in diameter. Viruses carry genetic viral material, composed of either DNA or RNA, encapsulated within a protein capsid, which protects the genome from the extracellular environment. The protein capsid is in many cases enclosed within a lipid membrane that is derived from the outer plasma membrane of host cells or from one of the inner cellular membranes. Viruses are incapable of self-replication, but rather ‘hijack’ the replication machinery of cells by attaching and penetrating the cellular membrane and mixing their genetic material with the host cells genome [92]. In doing so, replication of the viral genome is facilitated and consequently the host cell is turned into a virus factory. Some viruses can even cause permanent genetic changes of infected cells, leading to the development of cancer and other debilitating diseases [93]. One such highly infectious viruses, which has infected over 67% of the global population, is the membrane-enveloped herpes simplex virus type 1 (HSV-1) [94]. In this thesis work, preliminary attempts were made to investigate HSV-1 with respect to the dependence on membrane staining as a function of virus size (see the Future outlook chapter).

1.4.2 Extracellular vesicles

Extracellular vesicles (EVs) are cell-secreted vesicles capable of carrying different cargo, such as lipids, proteins, DNA, mRNA and miRNA and are present in all body fluids [8,95]. These

nanovesicles have been identified to play an important role in a variety of biological processes, including pathological conditions such as cancer and different neurological conditions, and have even been proposed to represent a common route for transport of neurodegenerative disease-related proteins and nucleic acids [2]. Specifically, transfer of proteins via exosomes from diseased cells to healthy cells frequently leads to accumulation and aggregation of the protein in the target cell, which is linked to the pathogenesis of many neurodegenerative diseases, such as Alzheimer's [2].

EVs are heterogeneous both in size and composition, with sizes ranging from 30 nm to 1 µm [96]. EVs include distinct subtypes such as exosomes, microvesicles and oncosomes (released by cancer cells) [97]. Exosomes are EVs produced in the endosomal compartment of most eukaryotic cells. They contain miRNA and mRNA, have been shown to transfer their genetic content, which upon delivery can be translated to proteins by the receiving cells [98]. There are also reports suggesting that EVs can in fact spread viral cargo such as HSV-1 in their envelope, which can be taken up by healthy cells, leading to viral infection [10]. Furthermore, studies have demonstrated that EV release kinetics from cancer cells varies considerably compared with healthy cells [9]. Therefore, EVs serve as promising biomarkers for a multitude of debilitating diseases. Due to their capacity to deliver biomolecular cargo, they may also guide the development of novel therapeutic delivery systems based on their mode of action.

Consequently, in order to determine how these BNPs mediate biological processes and how EV malfunctioning contributes to the development of neurodegenerative and other diseases, there is a need to develop effective bioanalytical tools for improved characterization of BNPs. Despite the existence of several bioanalytical tools for investigations of single nanoparticles, which will be introduced in the next chapter, precise determination of both size and content of each individual EV has proven to be a challenge [12]. Measurements of EV size distribution in relation to their membrane content was investigated in Paper IV.

1.4.3 Native membrane vesicles

Since EVs and exosomes vary significantly in composition, based on the producer cell type [99], and exhibit complex structures that are difficult to characterize, simpler systems are helpful for the development of new single nanoparticle analytical tools. Native membrane vesicles (NMVs) are one such simplified BNP systems that can be produced *in vitro* from the plasma membrane of a cell. NMVs retain the membrane components of the parent cell: lipids, proteins, carbohydrates [100,101]. Hence, the membrane of NMVs closely mimics the

membrane composition of exosomes, since it is also derived from the host cell which it was released from [2,23]. However, unlike exosomes, NMVs are easy to produce from host cells with several simple ultracentrifugation steps [100], while still acting as a more closely related exosome model compared to synthetic vesicles. These simpler, native BNPs were in this thesis work utilized as a model system that acted as a precursor for EV and exosome characterization. Specifically, the size determination of NMVs in relation to their membrane content were compared to that of EVs and synthetic vesicles in Paper IV.

2 Single nanoparticle analytics

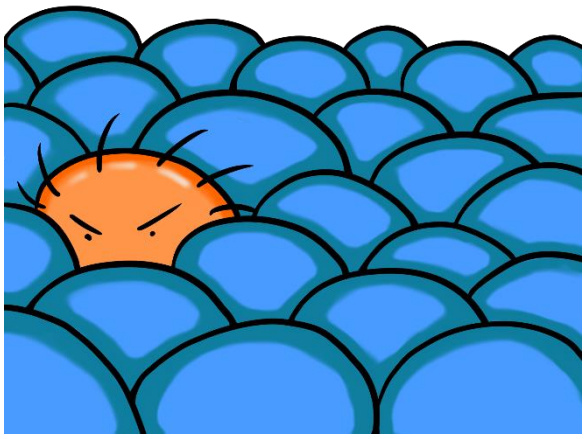

Even though human height is measured in meters, the building blocks of life are in the length scale of several nanometers to a few microns. For example, a typical red blood cell is around 8 µm, viruses which infect cells are around 100 nm, whereas the thickness of the cell membrane, which the virus attaches onto and subsequently penetrates, is around 5 nm. For reference, this is about a billion times smaller than the height of an average human. This chapter introduces the reader to the most common methods to study single biological nanoparticles.

As mentioned in the previous chapter, a multitude of quantitative methods exist to characterize BNP properties. The predominant technique for the last few decades to gain insight on a particle's physical properties has been electron microscopy. However, certain limitations, especially with respect to cumbersome sample preparation, low throughput and high costs, have called for the development of complementary techniques. This chapter provides an overview of the most commonly used BNP characterization methods (Table 1).

Electron microscopy (EM) allows a direct read-out of both size and structural properties. Images in EM are created from accelerated electrons, that after being transmitted or scattered by the sample under investigation hit an electron detector. The short wavelengths of electrons translates into sub nm resolution [102] when used to probe structure. As EM experiments are conventionally performed in high vacuum, and since liposomes, virus particles and other BNPs do not withstand dehydration, metal staining and chemical fixation techniques are often required, which may in turn change the size and morphology of the sample [103]. This limitation can be overcome by using cryo-electron microscopy (cryoEM), which circumvents both staining and fixation protocols. Instead, a thin film of the NP suspension is spread on a EM support grid and thereafter submerged into liquid ethane [104], which rapidly freezes the water into amorphous ice without forming ice crystals [105]. This process both preserves the material in a native-like state and protects the sample from radiation damage. CryoEM has been employed successfully to characterize individual viruses [103], vesicles [106] and EVs [107–109], providing insights on both their structural properties and size. In addition to direct

structural information, labelling of EVs with antibody-modified gold nanoparticles has been employed to identify sub-populations in the EV preparation [108]. However, the low throughput, complicated sample preparation protocols, long measurement times, and high cost are all limiting factors for cryoEM to become a standard BNP analysis tool [110].

Atomic force microscopy (AFM) is another high-resolution method, which in contrast to cryoEM can be carried out at room temperature and in liquid-phase/wet conditions. In AFM, a surface is scanned with a very sharp tip (down to a few nanometers in width) coupled to a sensitive cantilever. The attractive or repulsive forces between the sharp tip and the surface deflect the cantilever. Since the bending constant of the cantilever is known, the force applied on it can be estimated from the magnitude of the reflection and a topographic map of the surface at sub-nanometer resolution [111]. AFM has thus been used to characterize the size of various EVs [112,113]. The immobilization of BNPs on a surface may nevertheless still impact structural integrity thus rendering it rather difficult to estimate the size for BNPs and other soft materials. A core limitation of both AFM and EM with respect to high variance, stems from their small sample utilization, especially for heterogenous EV samples, as only a few images can be captured in a reasonable amount of time. These time and cost limitations have largely triggered the search for higher throughput approaches [109].

Certain properties of nanoscale objects can be extracted using light-based methods. One such method is flow cytometry (FCM), which is used routinely to analyze single cells and smaller particles in the sub-micrometer range [114]. In FCM, cells or particles in a hydrodynamically-focused fluid stream are illuminated by a laser. Ideally, each cell or particle passes the laser beam one at a time, from where the scattering and fluorescence signals are measured. The structural information obtained from light scattering, although limited compared with that obtained using EM, can thus be correlated with biomolecular composition via immunolabeling using specifically bound fluorescently labeled antibodies [115]. The measured optical signal is dependent on both the size of the particle and its refractive index, and drops dramatically with reducing radius. This signal reduction with size makes the detection of sub-wavelength particles very demanding [116]. As a result, the majority of conventional cytometers only detect individual polystyrene beads with a size larger than ~300 nm [102,109], while sub-200 nm BNPs, such as viruses and exosomes, remain at the detection limit of conventional flow cytometers due to their weak scattering signals unless fluorescent labeling is employed [117,118].

To meet this limitation, a multitude of other methods have been developed. Inspired by the ensemble averaging method, dynamic light scattering (DLS) [119], the possibility to track the motion of individual nanoparticles, and to deduce their size from their individual motion has been made possible due to the recent technological advances in imaging sensors. In DLS, a dilute suspension containing monodisperse NPs undergoing Brownian motion is illuminated with a focused laser beam [120]. The illuminated NPs scatter light in all directions, which due to their Brownian motion within the illuminated volume leads to temporal fluctuations that depend on particle size. Using DLS, the size distributions of NP ranging between a few nanometers to several microns can be determined [102], with an impressive limit of detection, down to about 1 nm [121]. Owing to its broad range of detectable sizes, DLS is used routinely as a high-throughput and sensitive method for accurate size determination [116]. However, for BNP which possess high molecular and dimensional heterogeneity, such as EVs, it remains difficult to accurately determine their size as the intensity fluctuations of the recorded signal, become predominantly influenced by the presence of larger particles [102].

Owing to the growing interest to investigate highly heterogeneous nanoparticle suspensions, nanoparticle tracking analysis (NTA) has become one of the most commonly used optical methods for nanoparticle size determination, especially for BNPs such as extracellular vesicles [114] and viruses [122], reaching down to the 50 nm size regime [123]. The underlying principle behind NTA is similar to that of DLS, where particles undergoing random motion in a suspension are illuminated by a collimated laser beam. The scattered (or fluorescent) light induced by the particles is then temporally imaged using an objective fitted to a conventional optical microscope, positioned above the sample [124]. However, in contrast to DLS, the imaging mode of NTA makes it possible to analyze the nanoparticles individually, allowing their size to be extracted from their Brownian movement. Unlike DLS, NTA copes better with polydisperse samples, however the quantitative determination of scattering and fluorescent intensities remain difficult to quantify, since the particles are free to diffuse in and out of the focal plane [117]. NTA was routinely used in this work for BNP size determination, and is discussed in further detail in the Experimental methods chapter.

The size from NTA has shown to correlate well with alternative methods, such as those based on resistive pulse sensing (RPS). RPS is an indirect method, where individual NPs passing through an aperture change the conductance of an electrolyte solution in which the particles are dispersed. In addition to size, it has been demonstrated that charge, concentration and approximate shape of nm-sized objects can also be measured [125,126]. A notable example

is its use to sequence DNA [127] and to quantify time-dependent increase in size for viruses [128]. However, since the aperture size for RPS must be comparable to the size of the BNP [129], it poses limitations on the heterogeneity and size range of the sample.

Since neither FCM, DLS, AFM nor NTA are best suited to unambiguously quantify multiple properties at the level of single nanoparticles, there exists a need for analytical concepts that enable multi-parametric analysis of individual BNPs. One such method is the two-dimensional flow nanometry (2DFN) developed by Block et al. [13], which offers a detection limit in the sub-30 nm range while simultaneously offering the possibility to quantify the scattering / fluorescence intensity by confining them close to a liquid-solid interface in a microfluidic setup. This method was further developed and used in Paper IV to quantify the efficiency by which BNPs can be labeled with membrane-specific dyes and in Paper V to investigate how the diffusivity of DNA-tethered vesicles depend on their size. Due to the central role of 2DFN in this thesis work, it will be presented more thoroughly in the Experimental Methods chapter.

Table 1 Comparison of the bioanalytical methods discussed in this chapter.

Method	Limit of Detection	Principle	Mode of measurement	Comments
CryoEM	~1 nm	electron transmission	direct, individual	arduous sample preparation, low statistics
AFM	<1 nm	force	direct, individual	arduous sample preparation, low statistics
FCM	200 nm	light scattering	indirect, individual	multi-parametric
DLS	1 nm	diffusion	indirect, ensemble	monodisperse samples, relative size
NTA	50 nm	diffusion	indirect, individual	polydisperse samples
RPS	30 nm	conductivity	indirect, ensemble	multi-parametric, monodisperse samples

3 Experimental methods

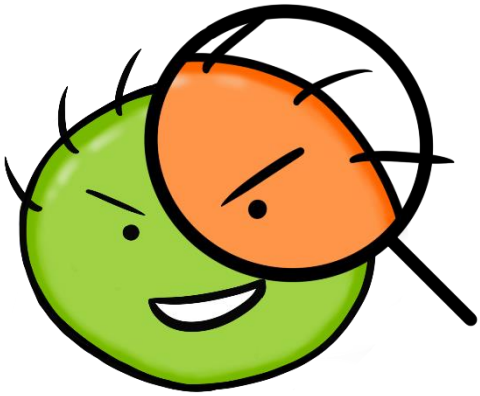

The interrogation of objects that cannot be resolved by the naked eye has for long been an integral part of the physical sciences. Among these techniques, optical methods have the broadest appeal due to the possibility to label biological systems with various markers, such as fluorescent dyes. This ability to track biological molecules, including proteins and lipids, has resulted in a vast array of notable discoveries in the fields of medicine and biology. The following techniques formed a basis upon which to build the novel nanoparticle analysis toolkit.

3.1 Fluorescence microscopy

Due to their small size, biological nanoparticles, such as lipid vesicles and other similarly sized objects, are not easily visualized directly with conventional optical microscopy. The most common method to increase their visibility is to attach fluorescent molecules, i.e., fluorophores[1]. Fluorophores are small chemical compounds that upon excitation can re-emit light. They come in various types and forms, can produce various colors and can in most cases be readily conjugated to other molecules such as lipids, allowing lipid membranes to be visualized. Alternatively, antibodies can be fluorescently labeled, which enables their unlabeled binding partners to be identified and visualized. The fluorescent molecule greatly increases the optical contrast between the labeled molecule and their surroundings, allowing different types of biomolecules to be detected and studied in a highly accurate spatiotemporal manner, even within cells, and more complex biological structures.

A fluorophore is a molecule which can absorb an incoming photon with an energy corresponding to the difference between the ground and first electronic excitation states. This photon energy absorption excites an electron in the ground state, S0, to the first excited singlet state, S1. This excited state is unstable with a short lifetime, typically in the range of 10^{-7} to 10^{-9} s. In order to lower its energy, the electron will relax down to the ground state either radiatively or non-radiatively, each with a certain probability. A non-radiative relaxation

[1] For a molecule to fluoresce, certain conditions have to be met, such as high rigidity of the molecule, the presence of electron-donor species, and naturally the molecule has to absorb the excitatory light and favor radiative transitions.

corresponds to all processes where the system relaxes without the emission of a photon, whereas the radiative process from S1-S0 with the re-emission of a photon is referred to as fluorescence [130]. Since a small portion of the absorbed energy is converted into vibrational energy, i.e., dissipated as heat, the re-emitted photon typically has a longer wavelength (lower energy) than the absorbed photon. This shift between the excitation wavelength and the emission wavelength of the fluorophore can be utilized for imaging purposes, which was a breakthrough discovery attributed to Oskar Heimstädt in 1911 [131]. An illustration of the phenomenon can be seen in a Jablonski diagram in Figure 4a [132]. The absorption process occurs on the order of 10^{-15} s, a process faster than molecular rearrangement and therefore the vibrational states do not change (Franck-Condon principle).

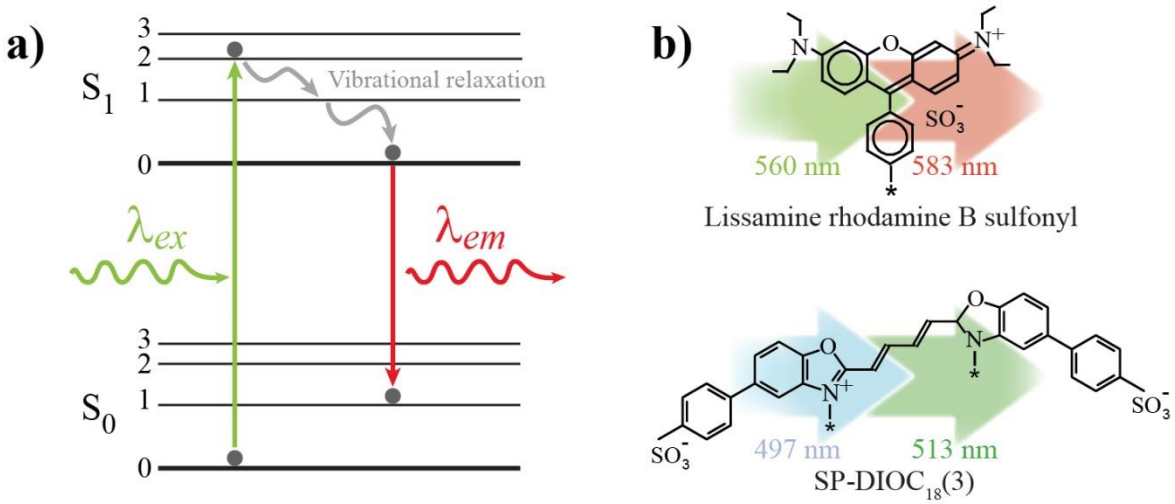

Figure 4. (a) A Jablonski diagram illustrating the concept of fluorescence on an energy plot. (b) Examples of two fluorophores used as lipid conjugated markers in this research – Rhodamine-DOPE and SP-DiOC$_{18}$(3) (only the fluorescing subunit is shown for clarity). Each fluorophore is overlaid with their typical excitation (left) and emission (right) wavelengths.

One of the key characteristics of fluorescent dyes is their quantum yield, which corresponds to the number ratio of the emitted and absorbed photons. Therefore, fluorophores which have a higher radiative to non-radiative rate back to the ground state, S0, also have a high quantum yield. Examples include bright dyes such as Rhodamine. The brightness of a fluorophore is also influenced by the overall relaxation rate to the ground state, which governs how rapidly the dye molecule is available for repeated excitations. The lifetime of fluorescence is the average time the molecule spends in the excited state prior to returning to the ground state. Typical fluorophores have lifetimes in the order of a few nanoseconds. Fluorophores with longer lifetimes will also have more time to interact with their environment while in the excited state, increasing the probability of non-radiative processes to occur. As the decay properties of

fluorophores can be influenced by their local environment, measuring these changes in their lifetime can offer valuable insight into their interactions with other surrounding molecules (e.g., other fluorophores).

A fluorescent molecule, being sensitive to its local environment, can thus have its emission suppressed or completely quenched. Fluorescence quenching refers to any process which decreases the fluorescence emission intensity of a given fluorophore. Quenching can occur via for example oxidation or energy transfer (of the excited state) to another molecule. Self-quenching is a special type of fluorescence quenching in which the fluorophore and quencher molecules are the same. When passing a given concentration threshold for a fluorophore, the relative distance between two molecules will become small enough (a few nanometers) so that their electronic and vibrational levels begin to overlap with each other, which allows energy transfer to occur between them, reducing or quenching the fluorescence signal. Thus, due to self-quenching effects, the addition of more fluorescence molecules will eventually decrease the ensemble intensity instead of increasing it [133]. Therefore, one must be careful in choosing the number of fluorophores to be used for each system.

Another important aspect of a fluorophore is its chemical stability. At high light intensities, a fluorophore will undergo many excitation-relaxation cycles. The stochastic nature of this process can have different outcomes. Since the dye molecule is more reactive in an excited state, it is probable that an absorbed photon can induce a chemical change in the fluorophore, which will result in a non-fluorescing (photobleached) state. Thus, in fluorescence microscopy, it is preferable to select dyes with superior photostability (in the order of ~1 million cycles), as high fluorescence quantum yield as possible and appropriate difference between the wavelengths of the absorbed and emitted light.

Many different kinds of fluorescence microscopy systems exist, including confocal laser scanning microscopy [134,135], super resolution microscopy such as stimulated emission depletion microscopy [136], and total internal reflection fluorescence microscopy [137], which was the main tool used for the research within this thesis.

3.1.1 Total internal reflection fluorescence microscopy

Total internal reflection fluorescence (TIRF) microscopy is an extension of conventional fluorescence microscopy, developed to illuminate only a thin layer directly above the substrate surface. This technique has been a prolific tool since its invention by Axelrod et al. during the

1980s [138] and is based on utilizing the evanescent electromagnetic wave formed at the interface between two optically transparent media of different refractive indices (n). When a beam of light travels from medium of high refractive index (n_{high}) to medium of lower refractive index (n_{low}) at an incident angle $\Theta_{\mathrm{incident}}$ larger than the critical angle $\Theta_{\mathrm{critical}}$, all light will be reflected at the interface. This mechanism is described by *Snell's law*, in the case where the angle of refraction becomes 90°:

$$\Theta_{\mathrm{incident}} > \Theta_{\mathrm{critical}} = \arcsin\left(\frac{n_{\mathrm{low}}}{n_{\mathrm{high}}}\right), \tag{3.1.1}$$

However, a non-radiative, evanescent, electromagnetic field confined at the interface is formed. This evanescent field slightly penetrates (a few hundred nanometers) into the medium of lower refractive index and decays exponentially with distance from the surface. The exponentially decaying light intensity I at distance z away from the interface can be described as:

$$I = I_0 e^{-\frac{z}{\delta}}, \tag{3.1.2}$$

where I_0 is the intensity of light at the interface and the distance where the light intensity has decayed $1/e$ times with respect to the value at the interface is called the penetration depth δ. The latter is defined as the following:

$$\delta = \frac{\lambda_0}{4\pi}\left(n_{\mathrm{high}}^2 \sin^2 \Theta_{\mathrm{incident}} - n_{\mathrm{low}}^2\right)^{-\frac{1}{2}}, \tag{3.1.3}$$

where λ_0 is the wavelength of the incident light [138]. As the light is totally reflected for angles $\Theta_{\mathrm{incident}} > \Theta_{\mathrm{critical}}$, the penetration depth of the evanescent wave can be adjusted by a few hundred nanometers by simply changing the incident angle $\Theta_{\mathrm{incident}}$ [139]. Using this evanescent light to excite fluorophores near the surface enables high contrast as the background signal of fluorophores from the bulk is significantly reduced.

In Papers II to V, an inverted TIRF microscope was used to image the sample from below, through a transparent borosilicate glass substrate (as shown on Figure 5). Lipid vesicles and SLBs were simultaneously imaged with this TIRF setup by using two different types of fluorescently-labelled molecules. The vesicles used in the experiments to form SLBs, were formed using a fraction of fluorophore-conjugated lipids (Rhodamine-DOPE or ATTO488PE), labeled at the hydrophilic head-group of the lipid. In Papers II-V only a fraction (1:100) of the vesicles were labelled for SLB formation to increase contrast between SLB patches and vesicles and thus enabling to monitor the SLB formation process. However, these lipid-dyes

cannot be used with native biological membranes without disturbing the membrane environment, as they need to be mixed in via sonication. Therefore, of particular interest is how lipophilic membrane-staining dyes, such as DiO and DiI, which have been utilized routinely to label cell membranes without negatively affecting membrane fluidity [140,141], incorporate into complex BNPs, and how this incorporation depends on particle size, type and molecular composition. Consequently, in Paper IV, small unilamellar vesicles (SUVs), native membrane vesicles (NMVs) and extracellular vesicles (EVs) were labelled with the lipophilic membrane-staining dye SP-DiOC$_{18}$(3)[2] (hereafter spDIO) which is weakly fluorescent in water but highly fluorescent and quite photostable when incorporated into a lipid membrane.

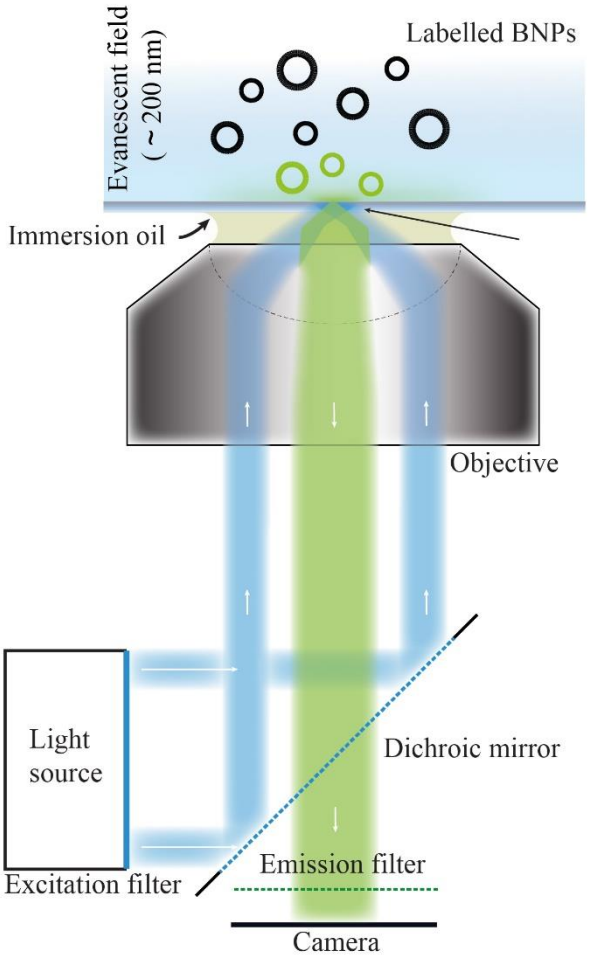

Figure 5. Diagram showing the working principle and main components of a TIRF microscopy. An off-axis light source is used to impact the sample at a large enough angle to fulfill the total internal reflection condition, resulting in the generation of an evanescent wave, exciting the fluorophores near the surface. A filter cube consisting of an excitation filter, dichroic mirror and an emission filter is present to select and direct the appropriate wavelengths for the fluorophore used and to isolate the fluorophore emission from the excitation source.

[2] 3,3'-Dioctadecyl-5,5'-Di(4-Sulfophenyl)Oxacarbocyanine

3.1.2 Confocal laser scanning microscopy

Confocal laser scanning microscopy (CLSM) is another fluorescence-based imaging method with high vertical resolution (~1.5 λ_o) compared to ordinary fluorescence microscopy. The first incarnation of a confocal microscope was invented by Marvin Minsky during the 1950s [134,135]. In conventional fluorescence microscopy, where the entire sample in the field-of-view is illuminated more-or-less evenly by the light source, both out-of-focus light from above and below the image plane is collected. In CLSM, a focused laser beam is scanned across the sample, whereas a pinhole eliminates most of light scattering from the out-of-focus sample points. Hence, at any given instant only one point of the sample is observed and the light intensities collected from each point are then reconstructed into an image, pixel-by-pixel. Since CLSM illuminates only a point of the sample at a time and features high vertical resolution, it is possible to construct three-dimensional images for which CLSM by also scanning the focus point vertically i.e., in the *z*-direction. The focal volume for confocal is larger than for TIRF microscopy, but since it is possible to have high accuracy in the *z*-direction, one can use it to select and focus on a thin slice further away from the surface, something that is not possible using TIRF microscopy. In Paper I, this unique property of CLSM was used to first focus on the BioPen (see section 3.2) enabling it to be positioned in a close proximity of a surface, and thereafter enabled to focus on the surface to monitor vesicle adsorption, membrane formation and spreading behavior.

3.1.3 Fluorescence recovery after photobleaching

In the context of lipid membranes, fluorescence recovery after photobleaching (FRAP) is an optical method, which makes use of the finite lifetime of fluorophores during high-intensity illumination to give insight on the lateral diffusion of fluorophores in a lipid membrane [142]. Specifically, a well-defined area of the sample is briefly exposed to a high-intensity laser beam, resulting in irreversible photobleaching of the fluorophores. This exposed area is seen as a dark spot under the microscope. If the lipids are able to diffuse e.g., in the case of a fluid lipid membrane, then the bleached fluorophore-conjugated lipids move out of the bleached spot and non-bleached lipids diffuse into the bleached area over time. The diffusivity of both bleached and non-bleached lipids leads to a fluorescence recovery of the previously bleached spot. By monitoring the extent and time of recovery with low-intensity light illumination, it is possible to estimate the diffusivity of the fluorophores, since a faster recovery is indicative of higher diffusivity and vice versa.

In Paper I, FRAP was used to measure the fluidity of deposited lipid patches. Whereas in Papers II-V, FRAP was used to confirm whether a fluid supported membrane was formed and still mobile after subsequent experimental steps.

3.2 Microfluidics and BioPen

Microfluidics, as the name states, is the manipulation of fluids in channels with dimensions in the range of micrometers (1-100 µm). The benefits of using microfluidics over traditional large volume bulk containers include, but are not limited to: (i) the ability to handle very small volumes of liquids (10^{-9} to 10^{-18} liters) and thus, reduce the consumption of samples, solvents and reagents, (ii) laminar flow (characterized by low Reynolds numbers), (iii) high resolution and sensitivity in separation and detection, and (iv) finely controlled flow rates and rapid exchange of liquids. These unique characteristics can be utilized to promote hydrodynamic shear flow that induces movement of molecules attached to an SLB [143], as discussed in Papers IV and V.

A simple straight microfluidic channel was fabricated from the optically transparent elastomer poly-(dimethylsiloxane) (PDMS) using soft-lithography; a simple fabrication method based on replica-molding from a predefined structural stamp [144]. This channel was used in Papers IV and V to enable controlled fluid flows, whereas simpler punched PDMS wells, conformally sealed to a support, were used in Papers II and III and throughout the thesis work for proof-of-concept measurements.

In Paper I, a multifunctional pipette, also made from PDMS called the BioPen [145] was used to produce lipid films with desired composition. The BioPen is a non-contact open-volume microfluidic device which can be loaded with several different vesicle suspensions. This pipette can then be submerged into the buffer and micromanipulated to being in close proximity to a surface of interest, which can then deliver an appropriate vesicle suspension. It utilizes a hydrodynamically confined flow (HFC) at the tip of the BioPen to create a confined solution droplet. Since this HFC region is dominated by laminar flow, then the circulating vesicle suspension does not mix with the buffer it is submerged in, but temporarily replaces the buffer with the vesicle suspension. The confined volume at the tip is maintained by means of positive pressure, injecting a fluid stream out of the tip into an open volume whereas negative pressures from adjacent channels, aspirate the solution back into the device, continuously re-circulating the solution and maintaining a constant concentration. Adjusting different pressure levels allows control over the speed, area and solution type, which will be delivered to the

surface. In Paper I, the pipette was employed to produce lipid films with desired composition on a variety of surfaces.

3.3 Size determination

A multitude of crucial interactions and functions of biological nanoparticles are based on their size. As a result, there is a need to develop sensitive and powerful particle size determination techniques that can detect sub-200 nm particles. Current state-of-the-art particle sizing technologies take advantage of the random thermal motion of particles, known as Brownian motion. This random movement of particles was first identified by Robert Brown when he observed small particles ejected from pollen grains undergoing continuous, random motion when dispersed in water. The particle's movement is characterized by rapidly changing velocities due to collision with solvent molecules, which are in constant motion with a thermal energy in the order of $k_{\mathrm{B}}T$. Collisions between dispersed NPs and solvent molecules occur in all directions and at all interfaces in a motion known as a *random walk*, first characterized by Albert Einstein in 1905 (Figure 6) [146]. Einstein determined that the Brownian motion of particles relate to their diffusivity, D, through their mean squared displacement (MSD), which is the measure of particle deviation from its reference position as a function of time [146–148]:

$$MSD(t) = \langle (\boldsymbol{r}(t) - \boldsymbol{r}_0)^2) \rangle = 2dDt\,, \qquad 3.3.4$$

where d is the number of dimensions (2 in our case), $\boldsymbol{r}_0$ is the reference position of the particle and $\boldsymbol{r}(t)$ the position at time t. The probability distribution of such a particle's displacement follows a Gaussian shape [146]. Here we should note the following assumptions: the mean free path of molecules is small compared to that of the particles [149]. We also neglect the inertia since t is large [150]. However, for small time scales one could potentially see the effect of inertia (since the particle movement would be visible between collisions).

Most commonly the MSD of an individual particle can be estimated from its experimentally measured trajectory for a given duration $n\Delta t$ (lag time) as follows [147,151,152]:

$$MSD(n\Delta t) = \frac{1}{N-n}\sum_{i=1}^{N-n}(\boldsymbol{r}_i - \boldsymbol{r}_{i+n})^2\,, \qquad n = 1, \ldots, N-1\,, \qquad 3.3.5$$

where N is the number of frames, $\boldsymbol{r}_i$ the particle position at frame i, whereas $\boldsymbol{r}_{i+n}$ the particle position after n frames and Δt the time interval characterized by the frame rate $1/\Delta t$.

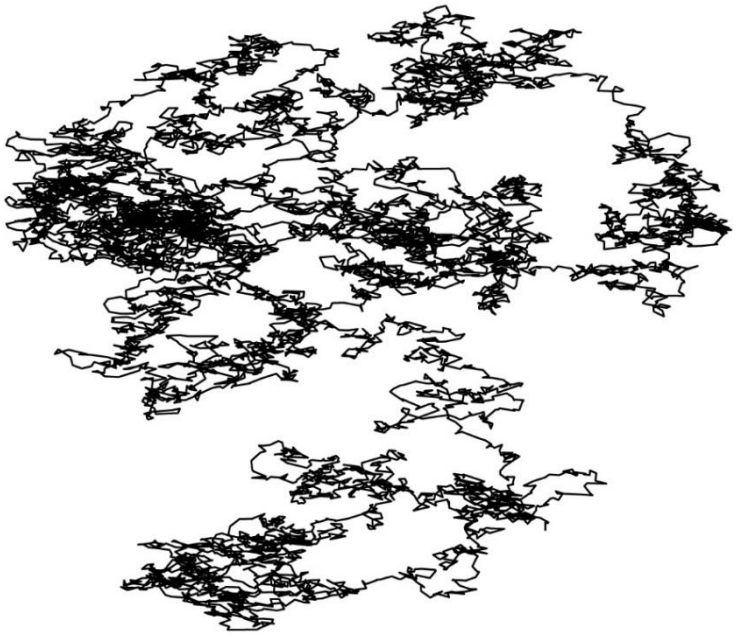

Figure 6. A simulated 2D random walk.

Einstein also showed, among others [153,154], how the aforementioned diffusivity relates to the mobility of a particle [146], which is known as the Einstein relation:

$$D = \mu k_{\mathrm{B}} T \,. \qquad 3.3.6$$

The mobility, μ, of a particle is the ratio between its drift velocity, v, and the applied drag force F ($\mu = v/F$), and is inversely proportional to the friction (drag) coefficient, ζ, which characterizes the influence of the surrounding medium. In the case of spherical particles at low Reynolds numbers [149], the Stokes's law [155] states that the friction coefficient is proportional to the (dynamic) viscosity, η, of the medium and the hydrodynamic radius, r, of the particle ($\zeta = 6\pi\eta r$). Thus, the Stokes-Einstein equation can be written:

$$D = \frac{k_{\mathrm{B}}\mathrm{T}}{6\pi\eta r}, \qquad 3.3.7$$

which shows that the diffusivity of a spherical particle depends (except for the thermal energy $k_{\mathrm{B}}T$), only on the viscosity of the solution and the hydrodynamic radius of the particle itself [146].

The aforementioned relation between the size and diffusivity of a particle (eq. 3.3.7) and the possibility to determine the diffusivity from the MSD of a particle's trajectory (eq. 3.3.4) are fundamental for the subsequent methods, as they enable to determine the hydrodynamic size of NPs from their trajectories.

3.3.1 Nanoparticle tracking analysis

Nanoparticle tracking analysis (NTA) is one of the most commonly used optical methods for nanoparticle size determination, especially for BNPs such as extracellular vesicles [114]. Conventional NTA uses a collimated laser beam to illuminate particles in a suspension. The particles within the beam scatter light in every direction. This scattered light by each particle in the field of view can then be collected by an objective placed above the sample, fitted to an otherwise conventional optical microscope [124]. The scattered light is captured by a high-speed camera, where the particles ongoing random movements in three dimensions will be visualized as bright/illuminated spots in the field of view. This facilitates individual identification and analysis of single particles by firstly calculating the diffusivity from its two-dimensional MSD (eq. 3.3.4). From this, the hydrodynamic radius (r) of each particle is extracted using the Stokes-Einstein equation (eq. 3.3.7) to reveal:

$$r = \frac{k_B T}{6\pi\eta D} \qquad 3.3.8$$

Since conventional NTA operates in scattering mode, with few instruments operating in both fluorescence and scattering mode [116], this size determination method is highly dependent on the optical properties (scattering cross-section) of the particles [156]. Consequently, materials with a refractive index significantly different from the dispersion medium (such as gold in water) are more easily detected than materials with a refractive index similar to the surrounding medium, such as lipid vesicles in buffer. Therefore, gold particles down to 30 nm can be detected whereas dielectric particles need to be somewhat larger (ranges from 70 nm to 1 µm [102,117] with rare examples of size determination down to 50 nm being possible [123]). The upper limit in size-determination is due to the inherently slow diffusion of particles larger than ~1 µm, which renders accurate size determination challenging.

Furthermore, there are additional limitations associated with detecting and quantifying particle size distributions using NTA. The trajectory of particles within the solution can only be accurately observed as a two-dimensional projection. However, within a solution, particles are free to move in three-dimensions, which causes particles to move in and out of the focal plane. This 3D movement of particles leads to significant errors in the position-determination since the scattering from out-of-focus particles appears dimmer than when they are confined within the focal plane. Such particles thus appear faint or are even lost from the field of view altogether during tracking. The effect of the latter is more dramatic for smaller NPs, which diffuse faster and have a lower intensity due to a smaller scattering cross-section. Furthermore,

particles that are out-of-focus may contribute to an increased background signal and particles that are moving in and out of the focal plane, may be re-counted by the algorithm, thus leading to a bias in the statistics of the size distribution.

In summary, although NTA can be utilized to estimate the size of NPs based on the fluorescence or scattering intensity, the accuracy of the method will be highly dependent on the signal intensity (contrast) and on how accurately the algorithm is able to determine the position of the NP, which should remain within the focal plane of the objective for as long as possible. The 3D movement of particles, however, leads to significant variance in the signal intensity, which can lead to unwanted artefacts and makes attempts to correlate intensity with NP size extremely challenging [157].

3.3.2 Two-dimensional flow nanometry

Some of the limitations associated with conventional NTA can be overcome by confining and restricting the movement of NPs within two dimensions. This was achieved recently by our group by coupling NPs to a fluid SLB, and thereby restricting the particles to the focal plane for a longer period of time [13]. This technique, known as *two-dimensional flow nanometry* (2DFN), improves the accuracy of both intensity and diffusivity estimations substantially, compared to NTA, allowing for precise size determinations of NPs 20-400 nm in diameter due to longer track lengths.

In order to couple BNPs to a fluidic interface, a linker, such as self-inserting cholesterol-modified DNA, must be inserted within the membrane of BNPs to allow for tethering to an SLB containing mobile complementary DNA (Figure 7). Due to this tethering approach, the theoretical principles used in NTA cannot be directly applied for 2DFN, as the lateral diffusivity of the linker-NP system is not primarily defined by NP size but rather by the slow diffusion of linker molecule in the SLB [90]. Specifically, the membrane friction experienced by the tethered particles is mostly defined by the number of linkers that are coupled to the fluid interface. Consequently, increasing the number of linkers between the NP and SLB will increase the membrane friction experienced by the linker, resulting in a decreased particle velocity. Since the diffusivity is reduced in the SLB, then in 2DFN it is possible to study the motion of fluorescently-labelled BNPs tethered to an SLB when subjected to a shear flow using a microfluidic channel. The applied shear force will scale with the particle size; thus, a larger force will make the BNPs move faster. In brief, by introducing hydrodynamic shear flow parallel to the SLB, the in-plane movements of BNPs can be monitored using total internal

reflection (TIRF) microscopy. In doing so, the individual size of the SLB-tethered BNPs can be elucidated by analyzing their trajectories when subjected to a shear flow [13], the physical principle of which is summarized below.

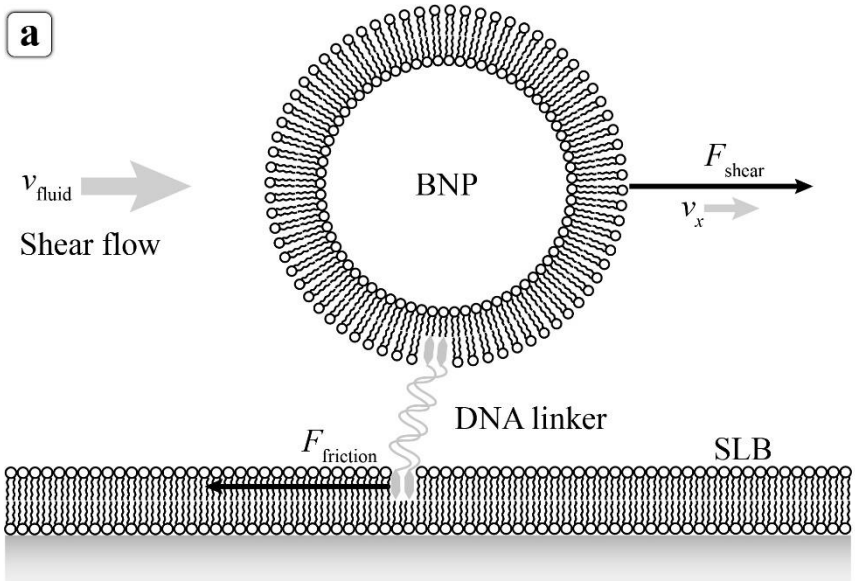

Figure 7. Simplified schematic of 2DFN depicting the main components of the system with the respective forces and velocities: F_{shear} is the relative force acting on the NP caused by the fluid flow velocity v_{fluid}, resulting in a net flow-directional velocity of v_x for the BNP. Whereas F_{friction} is the frictional force stemming from the linkers in the SLB resisting the movement.

When a bulk flow of liquid is applied above a planar SLB, the lipid bilayer and its constituents move in the direction of the bulk flow [158] and different sized components move with markedly different velocities. The friction coefficient, ζ, of a particle can be deduced from a laminar bulk-flow-induced shear force F_{shear}, which creates a directed movement of the particle in direction of the flow [146]. Hence, it can be inferred that a larger force will cause an increase in the particle's velocity. In a system consisting of a NP tethered to a fluid SLB via DNA linker molecules, the major two forces acting in the system (Figure 7) can be described as:

$$F_{\mathrm{friction}} = \zeta_{\mathrm{DNA}} v_x \,, \qquad 3.3.9$$

$$F_{\mathrm{shear}} = \zeta_{\mathrm{NP}} (v_{\mathrm{fluid}} - v_x) \,. \qquad 3.3.10$$

These forces are proportional to the friction coefficients ζ_{DNA} and ζ_{NP}, where F_{shear} is the relative force acting on the NP caused by the fluid flow velocity v_{fluid}, resulting in a net flow-directional velocity of v_x for the NPs, and F_{friction} is the frictional force stemming from the linkers in the SLB resisting the movement. It should be noted that the flow-induced motion of

the SLB is negligible at the volumetric flow rates used in this work. When the NP reaches equilibrium velocity these two forces are opposite and equal in magnitude:

$$F_{\text{friction}} = F_{\text{shear}} \,. \tag{3.3.11}$$

Therefore, by combining equations 3.3.9 and 3.3.10 we get:

$$\zeta_{\text{DNA}} v_x = \zeta_{\text{NP}}(v_{\text{fluid}} - v_x) \Leftrightarrow v_{\text{fluid}}\zeta_{\text{NP}} = v_x(\zeta_{\text{DNA}} + \zeta_{\text{NP}}) \,. \tag{3.3.12}$$

Furthermore, the fluctuation-dissipation theorem states that the forces that cause random fluctuations in a system at equilibrium, also create dissipation/friction when the system is subject to a non-random force [159]. In our context, the non-random drag force in the system creates a directed movement of the NP whereas the dissipation is related to the diffusivity of the NP and the tether system. By assuming that the frictions are additive in such a multi-component system, then $\zeta = \zeta_{\text{NP}} + \zeta_{\text{DNA}}$.

Therefore, according to Einstein's relation (eq. 3.3.6), the friction coefficient ζ (inverse of mobility) is also related to the diffusivity of the NP-linker system [146]:

$$\zeta = \frac{k_{\text{B}}T}{D} \,. \tag{3.3.13}$$

Thus, the movement of a NP tethered to an SLB under an applied shear force can be divided into two components: (i) directed, non-random NP movement in the flow direction induced by the shear force, and (ii) random movement perpendicular to the flow due to lipids diffusing and interacting with the linker in the membrane. Combining the previous equations 3.3.12 and 3.3.13 yields:

$$v_{\text{fluid}}\zeta_{\text{NP}} = \frac{k_{\text{B}}T v_x}{D} \,, \tag{3.3.14}$$

with the left side of equation 3.3.14 being simply the shear-force on the particle and is given by Stokes's law ($\zeta_{\text{NP}} = 6\pi\eta r$) [155]. Hence the expression can be reduced to:

$$\underbrace{6\pi\eta r v_{\text{fluid}}}_{\text{Stokes}} = \underbrace{(k_{\text{B}}T v_x)/D}_{\text{measured}} \,, \tag{3.3.15}$$

where η is the dynamic viscosity of the surrounding medium, v_x the average velocity of the particle. Here it is important to note, that since the force on the left side of equation 3.3.15 contains no tether dependence, then v_x and D on the right side will cancel out tether dependency and thus the force acting on the particle can be extracted directly.

By measuring the individual trajectories, i.e., MSD of tethered NPs in the *xy*-plane as a function of time, the diffusion coefficient, D, can be evaluated by studying the NP's *y*-position (Figure 8, bottom left), while the flow-directional velocity (v_x) of the NP can be deduced by studying the NP's *x*-position (Figure 8, bottom right).

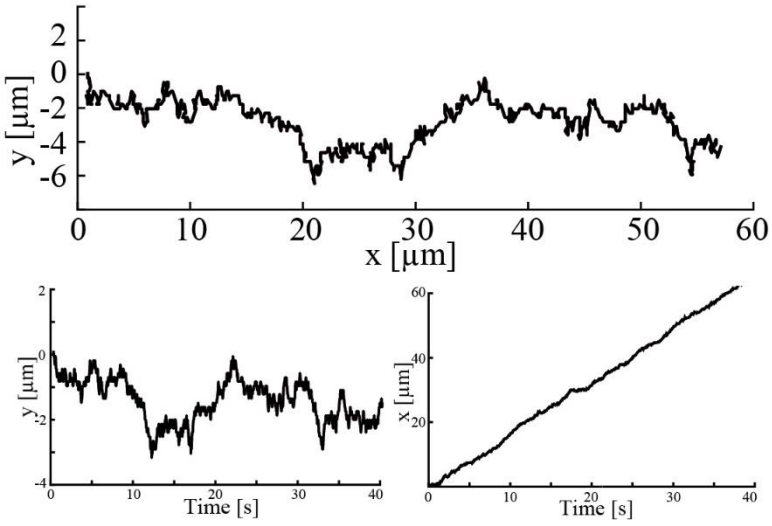

Figure 8. Characteristic track of a tethered BNP, showing the x-directional motion being dominated by a directed movement while the y-directional motion follows random Brownian motion.

Although equation 3.3.15 is valid for a simple system, some assumptions will still need to be made to determine the size distribution of NPs tethered to an SLB. This is because for fluids with non-zero viscosity, v_{fluid} is strictly speaking position dependent. For laminar flow, the velocity profile of the fluid will have a parabolic shape with maximum velocity in the center of the channel and lower at the walls, floor or ceiling [160]. However, close to the surface and over short distances, the velocity profile can be approximated by a linear function ($\frac{\partial v_{\text{fluid}}}{\partial z} = u_0$) [158,161–163] as seen in Figure 9a. Furthermore, it is usually assumed that the flow velocity of a viscous fluid close to a surface is zero, as mass cannot penetrate the solid surface and the cohesive forces between the molecules of the fluid are overcome by their adhesion to the surface [160]. However, there are several reports claiming that this so-called "no-slip" boundary condition is not strictly valid in all scenarios [164–167], thus a slip length must be introduced into our equations. The slip length λ can be described as an imaginary distance below the surface where the no-slip boundary condition would otherwise be satisfied while assuming a parabolic flow profile (Figure 9a) [167] and can also include the length of the linker molecule. Taking these two assumptions into account, the flow-directional velocity v_{fluid} at the center of the tethered NP of radius r, can be presented as:

$$v_{\text{fluid}} = u_0(r + \lambda)\,, \tag{3.3.16}$$

Consequently, by combining equations 3.3.15 and 3.3.16, the force F_{measured} acting on a particle in a 2DFN experiment can be determined via:

$$F_{\text{measured}} \equiv \frac{k_B T v_x}{D} = 6\pi\eta r v_{\text{fluid}} = A\eta u_0 r(r + \lambda) \tag{3.3.17}$$

where A is a constant that accounts for the channel geometry and inhomogeneous flow profile around the NP. It should be noted that both A and λ can be determined via calibration with NPs of known size for a specific channel geometry.

Thus, by measuring the individual trajectories of BNPs, the flow-directional velocity of a nanoparticle (v_x) and the average diffusivity of the NP-linker system (D) can be found. Consequently, if the latter two are known, the hydrodynamic force acting on each tracked NP can be directly determined via eq. 3.3.14. The shear force, along with the determined calibration parameters, can subsequently be used to determine the hydrodynamic size of the bound nanoparticles without directly probing a signal proportional to their size (Figure 9b).

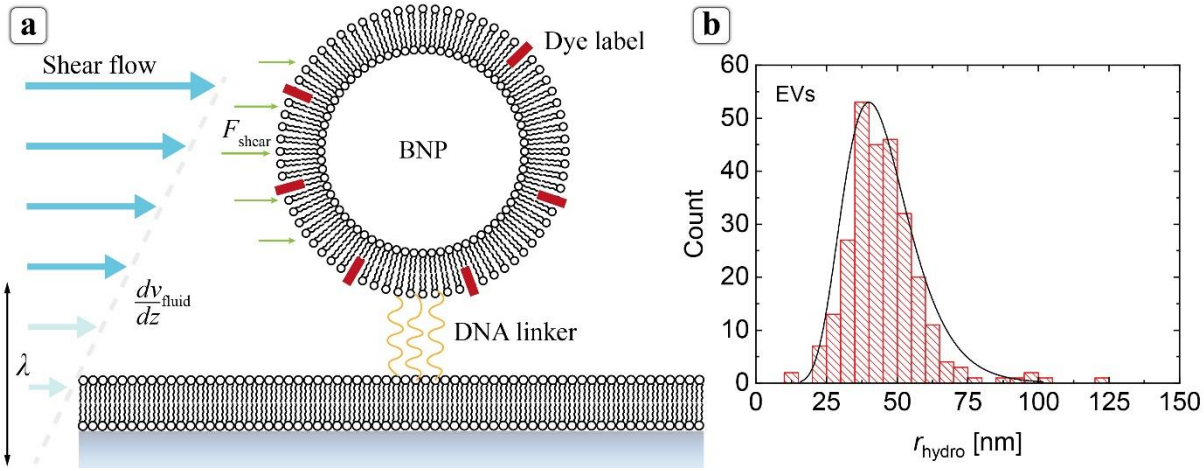

Figure 9. (a) A BNP tethered to an SLB via DNA linkers, experiencing a laminar shear flow causing the particle to move in the flow direction. λ indicates the slip length. (b) EV size distribution acquired with 2DFN.

2DFN offers several key advantages as a size determination technique, compared to conventional NTA. One clear advantage of 2DFN is the ability to accurately quantify the fluorescence intensity of BNPs. This is achievable since in the TIRF microscopy setup, the BNPs are confined to the surface during measurements, which allows to accurately probe the intensity of those fluorescently labeled BNPs that are coupled to the surface. Therefore, it is possible to correlate the fluorescence intensity of BNPs to their independently determined size.

For example, for BNPs with a homogenous surface dye concentration such as vesicles containing lipid-conjugated dyes, the TIRF intensity is expected to be proportional to their size [168]. However, it is speculated that dye distribution is commonly inhomogeneous in more complex biological systems, such as viruses and exosomes, where lipid-conjugated dyes cannot be used. Thus, in Paper IV, the 2DFN technique was used to determine the size, independent of fluorescent intensity, of the following BNP systems: artificial lipid vesicles, NMVs and EVs (Figure 9b).

3.3.2.1 Hindered diffusion

It has been previously demonstrated that fluorescence microscopy combined with single particle tracking can resolve the different number of cholesterol-DNA linkers, based on the diffusivity of vesicles tethered to an SLB [169]. However, in diffusion measurements for linked NPs the contribution of the vesicle is often assumed to be negligible. Under the assumption that the frictions are additive the contributions of the NP-linker system can be written as:

$$\zeta_{\Sigma} = N\zeta_{\text{linker}} + \zeta_{\text{NP}}\,, \tag{3.3.18}$$

where, N specifies the number of linkers between the NP and SLB, whereas ζ_{linker} and ζ_{NP} are the friction coefficients of a single linker and tethered NP, respectively. Thus, if the number of tethers is known for a certain NP size distribution and if ζ_{linker} is independent on BNP size, then the two contributions can be separated by using 2DFN, which enables simultaneous measurements of the diffusion and size of the NP-linker system. However, to be able to directly categorize the vesicles into classes containing a certain number of tethers, the effect from an additional tether must be large enough, so that the relative change in diffusion is larger than the spread in measured diffusivities.

The diffusion of a particle near an interface is different compared to bulk, and is influenced by its distance to the interface. The correction imposed on the hindered lateral diffusivity D of a NP due to the presence of a wall can be expressed as [150]:

$$D \approx D_{*}\left[1 - \frac{9}{16}\frac{r}{r+\lambda} + \frac{1}{8}\left(\frac{r}{r+\lambda}\right)^{3} - \frac{45}{256}\left(\frac{r}{r+\lambda}\right)^{4} - \frac{1}{16}\left(\frac{r}{r+\lambda}\right)^{5}\right] \tag{3.3.19}$$

where λ is the slip length (Figure 9) and D_{*} is the free diffusion in bulk. Thus, by investigating how the diffusion of the tethered NP scales with size, we can get information on the slip length. These aspects were studied in Paper V by using SUVs with a few numbers of tethers, to determine the drag contribution from the SUV and to estimate the slip length.

3.3.2.2 Data analysis

The data analysis of 2DFN is very sensitive to several parameters, which will be discussed more thoroughly below.

One such parameter is the *distance cutoff*, determining whether it is a unique particle that is being followed, i.e., if it belongs to a unique track, which is defined by a maximum distance between two 'particles' in two consecutive frames. This value is dependent on the surface coverage of the particles, since to avoid linking of two different particles in close proximity, the cutoff must be lowered when the density is high. This value is selected by using a large distance cutoff and plotting all mean squared displacements. By linearly fitting the initial data points, it is possible to evaluate where the true tracks meet the noise (the false linking events). This intersection (Figure 10) then defines the cutoff value that is used in the analysis.

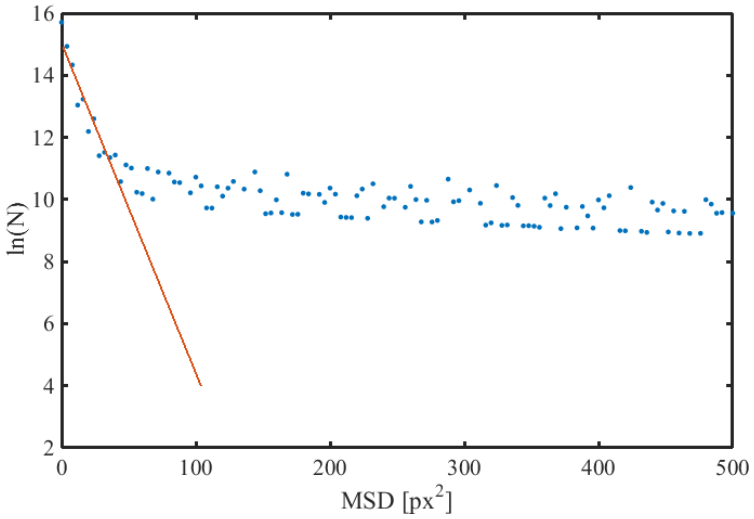

Figure 10. Logarithmic representation of the normalized count as a function of MSD. The cutoff value is evaluated at the intersection where the linear fit (red line) crosses the average noise, which in this case is 50.

For accurate intensity determination, multiple parameters which help to mitigate the influence of potential bleaching and other factors, must be chosen very carefully, since the resulting intensity distribution can be affected by several factors, such as uneven illumination, tracking errors, dye transfer to the SLB and mode of illumination (TIRF vs. EPI). Due to the aforementioned factors, the intensity of an individual particle can fluctuate quite significantly along the particle trajectory as it moves across the field-of-view. Typically, the average intensity throughout the whole trajectory is measured, but this would result in unnecessary fluctuations. Therefore, to lower the fluctuations, the intensity was determined in the middle 100 px of the field-of-view, where the TIR light hits the sample and consequently results in the

greatest signal-to-noise. Furthermore, to remove any potential tracking errors, which cannot be excluded with the distance cutoff, e.g., the linkage of two particles that are in close proximity, tracks with unreasonably large fluctuations around their average intensity value were removed. This was done by first measuring the intensity over time for a few immobile particles per movie. The particle with the highest standard deviation relative to its mean value was used as an upper limit, to include everything below that value in the intensity versus size graph. Specifically, this relative standard deviation of the intensity ranged between 10-25%.

4 Summary of results

The majority of findings obtained in this thesis work are captured in five papers, which are summarized and detailed below. A few additional results are briefly summarized in the Future outlook chapter.

4.1 Paper I

Supported membranes are attractive cell membrane mimics, as well as excellent interfaces in sensing and implants. Since the type of lipid structure formed on inorganic surfaces is dependent on the structural and chemical properties associated with the substrate, it is fundamentally important to understand (i) what surfaces support lipid membranes, and (ii) the key surface characteristics that control membrane self-assembly. Accordingly, the application of supported membranes in the development of new sensors and devices incorporating lipid membranes is dependent on finding compatible lipid-surface combinations. In the context of this thesis, it was important to know which substrate-lipid combination will yield the most suitable membrane assembly for attachment of biological nanoparticles. Therefore, in Paper I, we employed confocal laser scanning microscopy (CLSM) to study vesicle adsorption and membrane formation on a multitude of biologically relevant microengineering materials. These optically transparent materials comprised of borosilicate glass, mica, SiO_2, Al (native oxide), Al_2O_3, TiO_2, ITO, SiC, Au, Teflon AF, SU-8 and graphene. A key component to facilitate this study was the BioPen [145], which enabled local deposition of small unilamellar vesicles (SUVs) containing various ratios of zwitterionic POPC and cationic DOTAP lipids. Using this microfluidic device, the SUVs were circulated in a hydrodynamically confined volume near the device tip in close proximity to the surface, which led to adsorption of the vesicles, under certain conditions being followed by vesicle rupture and formation of planar membrane films. Since the cationic nature of DOTAP affects membrane formation, we measured the surface potential for each surface and, to our knowledge, for the first time on graphene. The findings of this work are summarized in Figure 11. Typically, adhesion without immediate rupture was associated with a high fraction of POPC lipids while an increasing content of positively charged lipids rendered membrane formation and spreading increasingly favourable. In general, mono-, bilayer and double bilayer formation was observed depending on the lipid content and underlying surface. Since borosilicate glass facilitated formation of continuous fluid supported lipid bilayers irrespective of lipid composition, it emerged as the most ideal and robust substrate for membrane formation.

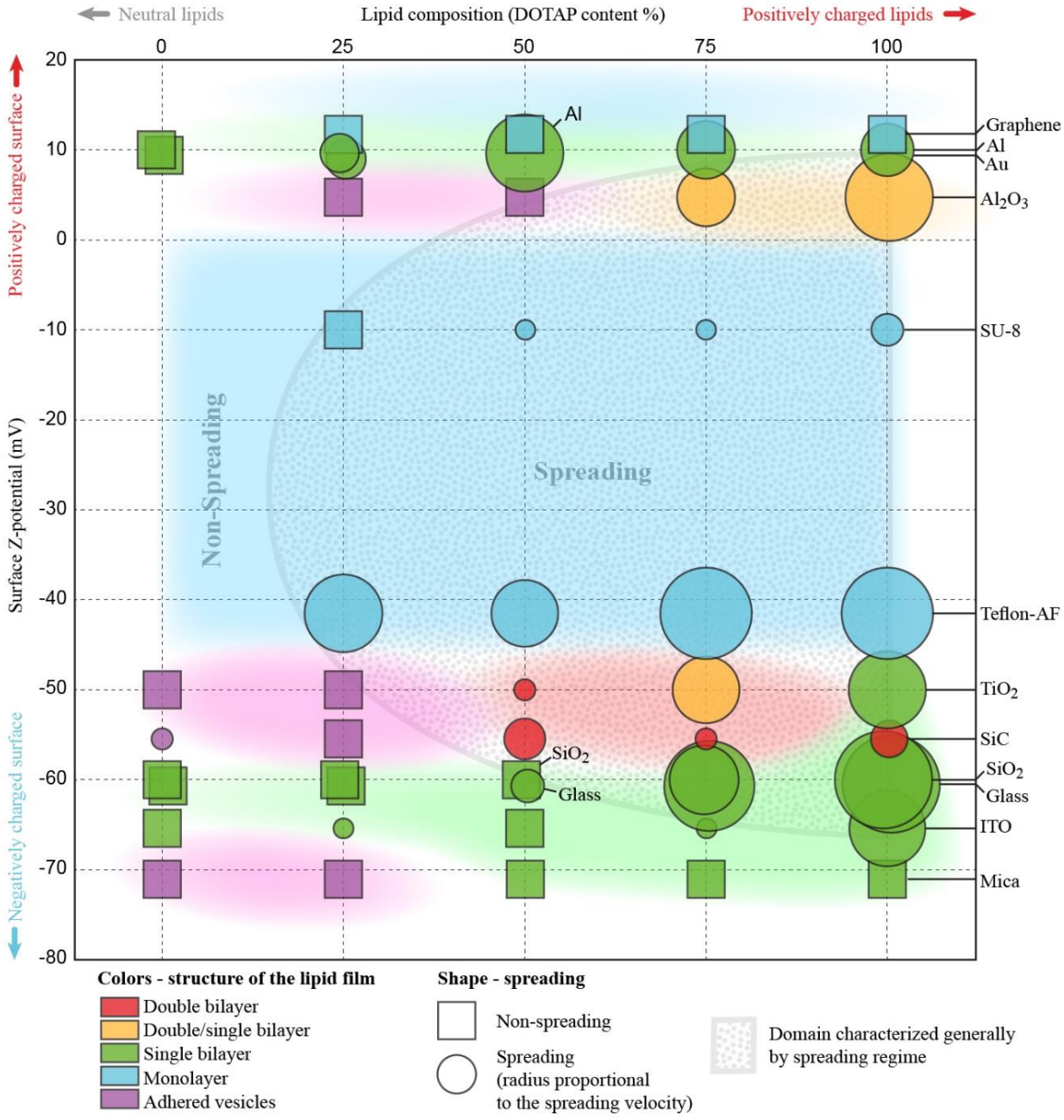

Figure 11. Diagram of lipid-surface interactions depending on the lipid composition and surface charge (displayed on the y-axis as Z-potential at pH 7.4). Colors represent different film structures, ranging from adhered vesicles (magenta) to mono-(blue), bi-(green) or double bilayer (orange and red) membranes. Shapes denote observed spreading (squares - non-spreading and circles - spreading films, while the diameter of the circles is proportional to the delta-spreading radius). Background shades are used to indicate approximate regions in the diagram, where certain behaviors are more dominant, even though there are exception to these general tendencies.

4.2 Paper II

Supported lipid bilayers (SLBs) mimic several key features of cellular membranes, such as planar geometry and lateral fluidity. In all studies concerning SLBs, the quality of the SLB is a critical factor that influences its function and utility. Therefore, significant efforts have been invested to gain an in-depth understanding of the SLB formation process [62,63,170–175]. Further, utilizing SLBs as a core of the measurement approach taken to characterize biological nanoparticles (Papers IV and V), places specific weight upon highly reproducible SLBs. Therefore, in Paper II, we employed TIRF microscopy to study SLB formation kinetics on borosilicate glass. In comparison to how fluorescence microscopy was previously employed to study SLB formation [176,177], we labelled only a small fraction (1%) of the vesicles, allowing the individual adsorbed vesicles and SLB patches to be monitored simultaneously, since in this way, vesicle rupture into SLB patches increased the optical contrast between the patches, adsorbed vesicles and uncovered regions of the surface [100]. Resolving individual vesicles allowed the entire SLB formation process to be observed, from individual vesicles to small SLB patches, and finally coalescence to a full SLB. To quantify the individual SLB patches and variations in patch-growth scenarios, the boundary of each patch was identified for each analyzed time point and subsequently used to calculate the average front velocity. It was concluded from our analysis that the average front velocity tends to increase dramatically, up to one order of magnitude, even though the surface density of adsorbed vesicles increases only marginally by about 8% (Figure 12). This finding is considered significant as typically the front velocity of a spreading lipid mono-or bi-layer front on hydrophobic and hydrophilic surfaces, respectively, is either decreasing or stagnant over time [39,42,45].

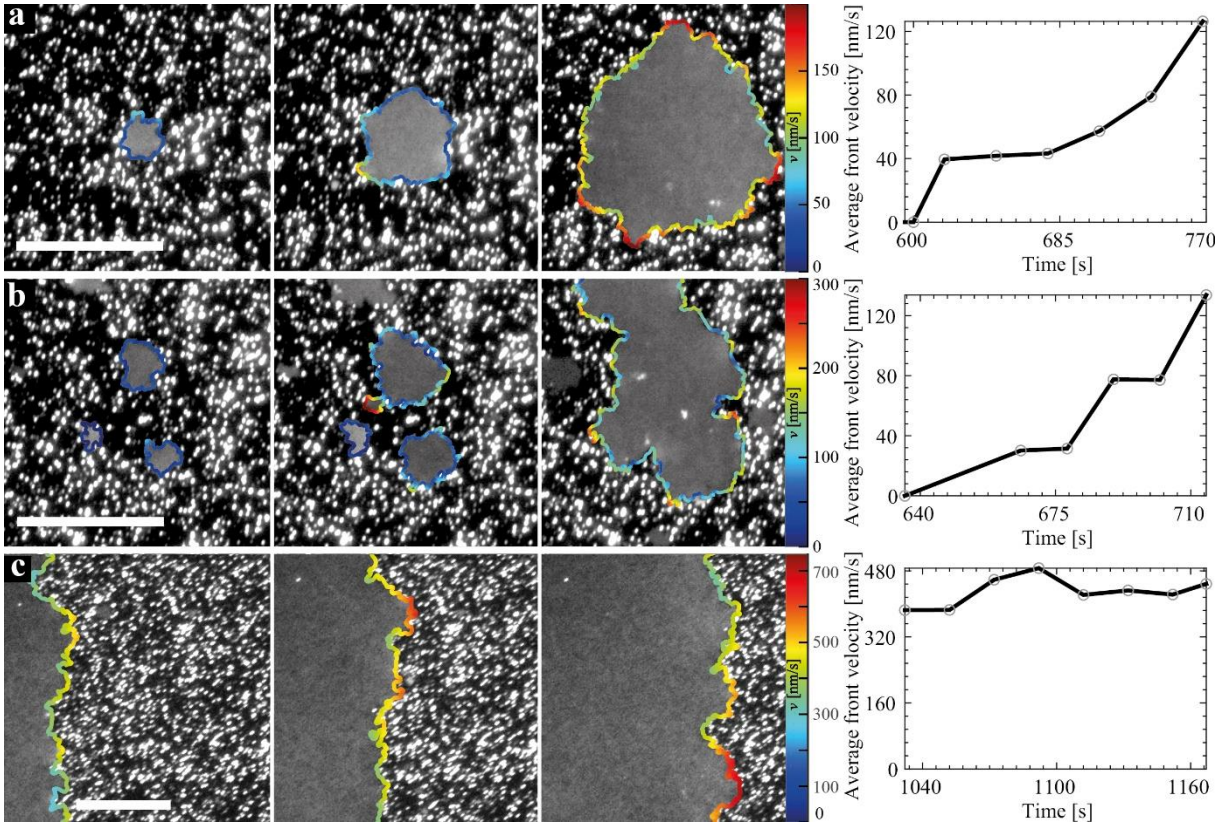

Figure 12. Typical patterns observed during the SLB patch growth and the corresponding dependence of the average front velocity with time: (a) single patch formation and expansion (snapshot interval 60 s), (b) small patches merging into a bigger patch (snapshot interval 24 sec), and (c) propagating SLB front (snapshot interval 30 sec). Scale bars represent 20 µm. The color of the perimeter lines used in the images, indicates the local front velocity of the SLB patch.

To theoretically address the rate of SLB growth, two different scenarios regarding the incorporation of lipids into the SLB patch after the rupture were examined: *local relaxation* and *global relaxation*. In the *local relaxation* scenario, the lipids belonging to a ruptured vesicle are assumed to form a circular SLB, where the growth is restricted to the immediate vicinity of each ruptured vesicle. In this scheme, no significant lipid rearrangement in newly-formed patches occurs, implying that the overlap with the existing SLB patches can be interpreted as either a double bilayer or material loss. In the *global relaxation* scenario, all lipids from ruptured vesicles will instead rapidly diffuse along the substrate and merge with the patch inducing their rupture, resulting in a circular SLB. The majority of the experimental observations followed the *global relaxation* model, manifesting in increasing front velocities (Figure 12). The global model also describes the observed cases, where the local coverage of vesicles was low. In these cases, the growth halted until more material for sustainable growth was introduced.

4.3 Paper III

A major challenge in oral drug delivery is the transport of drug molecules across the intestinal epithelia, which is limited by the aqueous solubility and permeability of the drug compound [178]. This is complicated by the fact that the major portion of newly-developed drug entities are poorly soluble and poorly permeable [179], which limits their oral absorption into the systemic bloodstream. Subsequently, it is of significant interest to investigate how poorly soluble drug molecules interact with lipid bilayers to simulate the absorption pathway across intestinal epithelia cells, especially when the drug is solubilized by exogenous lipid vesicles present in the gastrointestinal tract. Motivated by the SLB formation studies in Paper II, we devised a method in Paper III to monitor drug permeability through synthetic SLBs formed on a mesoporous silica thin film (MSTF) substrate. MSTFs were selected as the optimal substrate for this study since they (i) have previously been shown to be suitable supports for SLBs containing transmembrane proteins [82], and (ii) are highly porous substrates which introduces the ability to monitor drug diffusion across the lipid bilayer, into the silica mesopores. The integrity of the lipid membrane was verified using fluorescence recovery after photobleaching (FRAP), and it was found that POPC SLB adsorbed on MSTF exerted a ~2-fold greater diffusion rate compared to the POPC SLB on the flat silica substrate.

Importantly, since the MSTF was spin-coated on glass, it was possible to illuminate the sample at a greater angle of incidence, thereby restricting the evanescent illumination to within the MSTF only, i.e., below the SLB. In doing so, it was possible to monitor the time-dependent permeation of the model poorly water-soluble drug, felodipine, across the SLB by examining changes in fluorescence intensity within the MSTF (Figure 13). To solubilize felodipine and mimic the conditions in the small intestine, a fasted-state simulated intestinal fluid (FaSSIF) media was used, which contains a biologically relevant concentration of exogenous lipids that form micelles and other solubilizing colloidal vesicles [180]. The permeation behavior of felodipine was contrasted between (i) the pure drug, (ii) drug solubilized in fasted-state micelles, and (iii) drug solubilized in fasted-state micelles coupled with a widely used permeability enhancer, caprylic acid (C8). The change in fluorescence intensity associated with felodipine permeating across the SLB, into the MSTF pores, was insignificant for the pure drug, highlighting its poor solubility and inability for precipitated drug to diffuse across the SLB. When solubilized in FaSSIF, the fluorescence intensity within the MSTF pores was several times greater than the pure drug, indicating that felodipine is permeable in its dissolved form. However, of greatest significance, when felodipine was administer with FaSSIF and C8,

drug permeation was increased by a factor of 5 compared to FaSSIF alone, providing evidence for C8-mediated drug transport across a lipid membrane, while validating the potential for this approach to successfully quantify formulation-induced changes to drug-permeation.

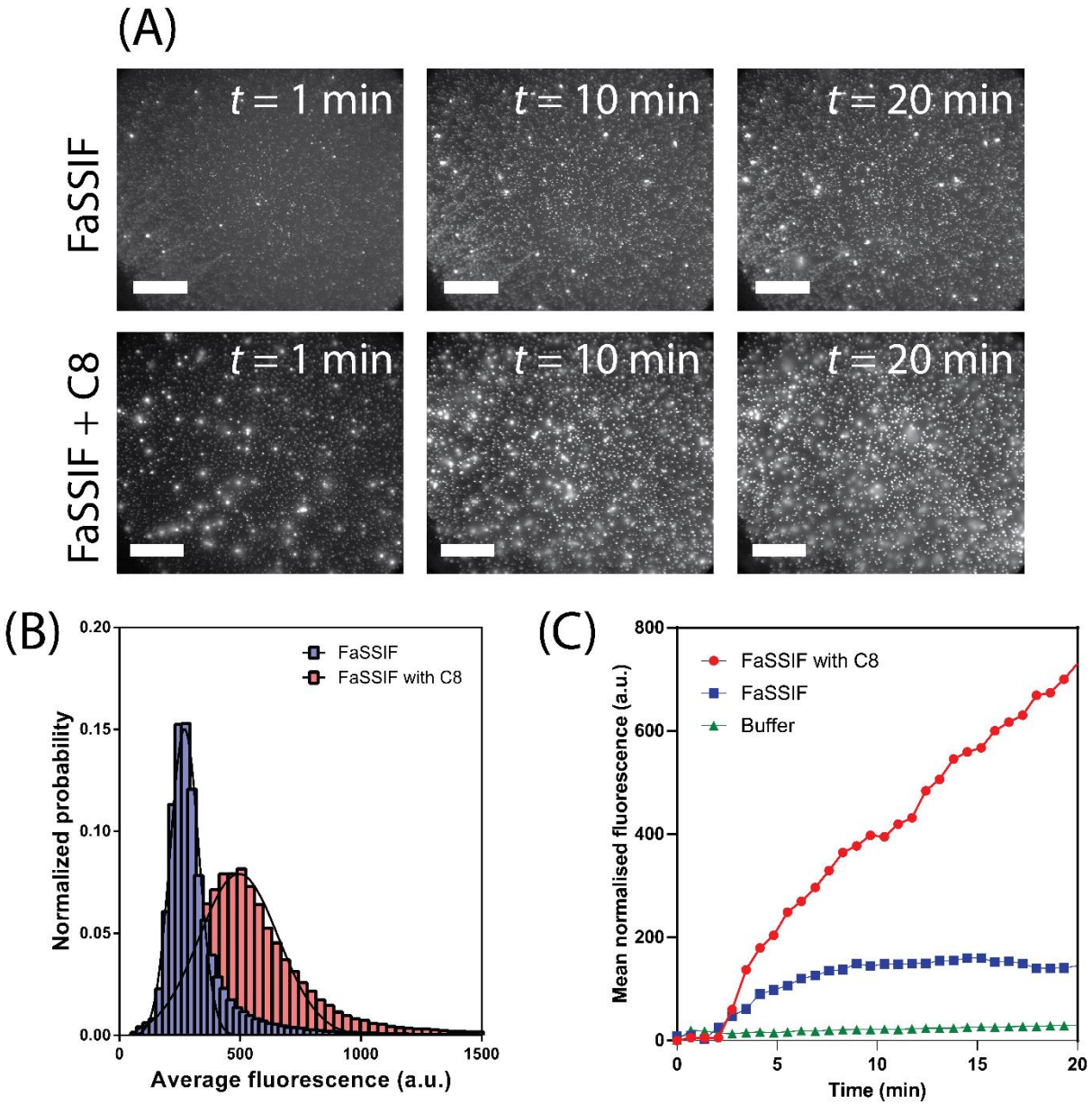

Figure 13. (A) TIRF micrographs at various time points highlighting felodipine permeation across the lipid bilayer into the pores of the MSTF, when solubilized within FaSSIF without a permeation enhancer (top row) and with C8 (bottom row). Scale bars = 20 µm. (B) Fluorescent intensity distributions, fit with a normal distribution, for felodipine patches within MSTF when combined with FaSSIF (blue bars) and FaSSIF with C8 (red bars). (C) Mean normalised fluorescence as a function of time for felodipine within MSTF when administered with buffer (green triangles), FaSSIF (blue squares) and FaSSIF with C8 (red circles).

4.4 Paper IV

The development and advancement of novel nanoparticle size determination and characterization techniques is integral for improved understanding of cellular processes involving biological nanoparticles (BNPs), such as cellular communication and viral infections [95,98,181,182]. Since BNPs are typically very heterogeneous, there is a demand for techniques that provide simultaneous information of multiple parameters, such as size and concentration, preferably with single BNP resolution. To achieve this, we used TIRF microscopy combined with microfluidics in Paper IV to study fluorescently-labelled BNPs with varying complexity tethered to an SLB. Two-dimensional flow nanometry (2DFN) was utilized in this approach by applying shear force to the vesicles, allowing for the Brownian motion of tethered vesicles to be decoupled from their directed motion. In doing so, the hydrodynamic size and fluorescent emission could be determined independently for each tracked BNP [13].

In previous work, it was verified that fluorescence intensity could be correlated to vesicle size for a fluorescent lipid-dye (Rhodamine-DOPE), which was incorporated during vesicle fabrication [13]. However, dye-labeled lipids cannot be incorporated into native biological membranes without severely disturbing the lipid organization, since they need to be introduced by lysing the membrane through sonication or similar. To this end, self-inserting lipophilic dyes originally developed for cell-membrane labeling have gained increased popularity for labeling of BNPs [183–186]. However, despite the extensive use of lipophilic dyes, it remains unclear how they are incorporated into complex BNPs, and how this incorporation depends on BNP type, size and molecular composition. In this paper, we therefore used 2DFN to explore the correlation between the dye incorporation efficiency and BNP size. Specifically, 2DFN was utilized to independently derive the size and fluorescence intensity of model BNPs with varying complexities, ranging from artificial vesicles to NMVs and EVs, using the lipophilic-staining dye, spDIO, which has been routinely utilized to label cell membranes without negatively affecting membrane fluidity [140,141].

It was shown that the fluorescent intensity of synthetic vesicles scaled with their membrane area, while for more complex BNPs, labelled with spDIO, the incorporation efficiency was significantly lower than for synthetic POPC and a significantly weaker dependence on size was observed (Figure 14). The latter observation is attributed to a size dependent difference in membrane composition, which may influence either the optical properties of the dye and/or the

insertion efficiency, indicating that the fluorescence emission of this type of self-inserting dyes may not serve as reliable probes to estimate the size of BNPs with complex lipid compositions. While the observed reduction in fluorescence intensity is attributed to lower incorporation efficiency, an influence on the fluorescence emission from membrane environment cannot be excluded.

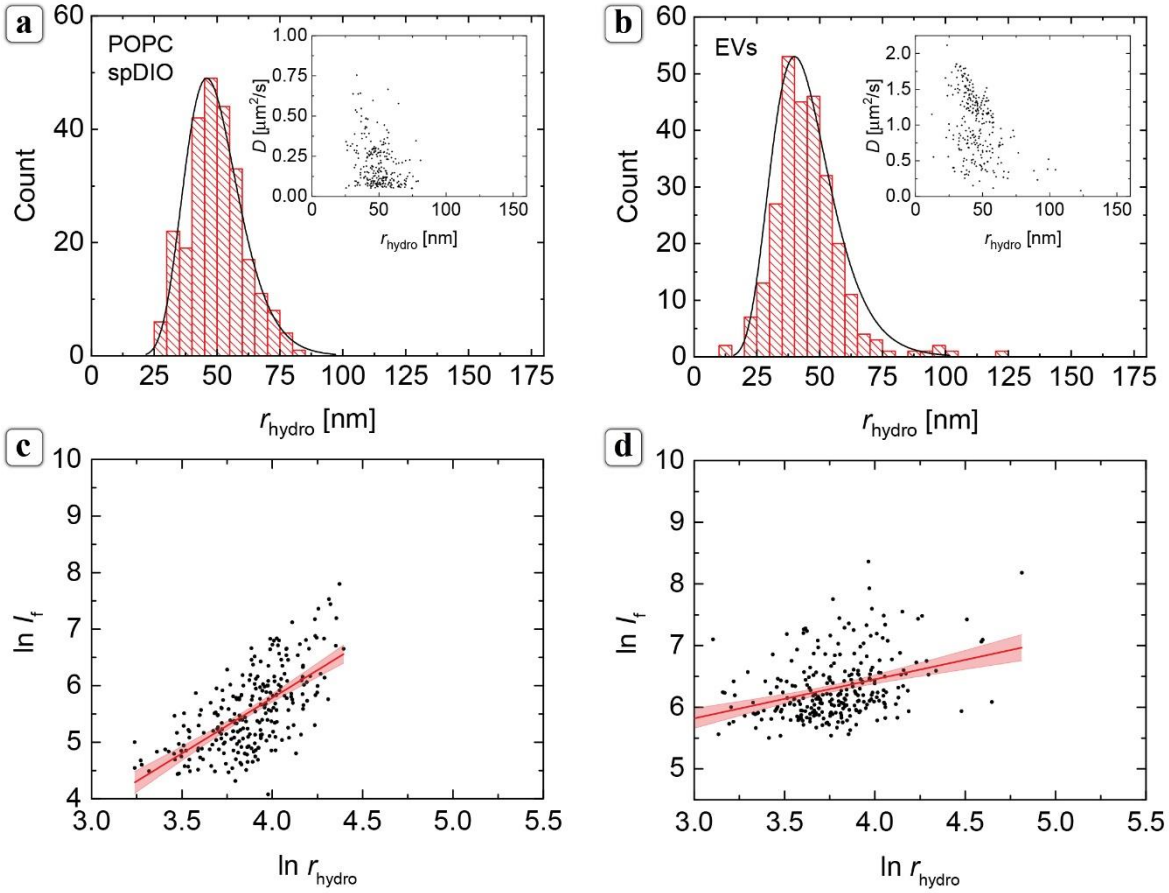

Figure 14. Size distribution determined using 2DFN of spDIO-labelled a) POPC vesicles and b) EVs with corresponding log-normal fits (black lines). The insets in a) and b) depict the spread of diffusivity in relation to the hydrodynamic radius of the BNPs. Fluorescence intensity versus hydrodynamic radius log-log plots for spDIO-labelled c) vesicles with a linear fit (red) of 2.0 ± 0.3 (with 95% confidence bands) and d) EVs with a linear fit (red) of 0.6 ± 0.2 (with 95% confidence bands, 10 cholesterol-DNA/BNP). Only tracks longer than 100 frames were used in the analysis.

4.5 Paper V

Multivalent interactions are widespread in biological processes, especially in the interaction between biological nanoparticles and cellular membranes [187,188]. Lipid vesicles tethered to SLBs offer a unique model system to quantify multivalent interactions in physiologically relevant conditions via the dependence of nanoparticle diffusivity on the number of discrete linkers [91,189]. More specifically, since it can be assumed that various friction contributions are additive, the inverse diffusion scales approximately linearly with the number of linkers and the size of the vesicle. However, in these systems the friction contribution originating from the size of the NP in the NP-linker system is often assumed to be negligible compared to the friction of the linkers. 2DFN, which was used in Paper IV, can test the limits of this assumption, since it enables to simultaneously investigate the diffusivity and size of the NP-linker system under controlled flow conditions. Thus, in Paper V, we employed 2DFN with small unilamellar vesicles (SUVs; r~30 nm) containing only a few cholesterol-DNA linkers to disentangle the contribution of the NP and tether from the total mobility of the system. When monitoring the diffusivity and velocity of a single NP, we observed that in the regime of few tethers, the data is spontaneously organized in clusters which are related to vesicles tethered with different numbers of linkers (Figure 15). Note that inverse diffusivity has been used here, because it makes the interpretation of the results easier as it is directly proportional the addition of friction terms in the NP-linker system, and helps to illustrate that the effect of the particle size of the NP-tether system should not be disregarded when the number of DNA tethers is 1 – 3. Furthermore, by changing the ionic strength of the system, it was observed that the relative ratio of vesicles for the various tether populations changes (Figure 15c). An additional result is that the diffusion coefficient of a single DNA linker for our case can be estimated to be 2 – 2.5 $\mu m^2/s$, which is reasonable in comparison with diffusivity values for single lipids within SLBs on a glass surface.

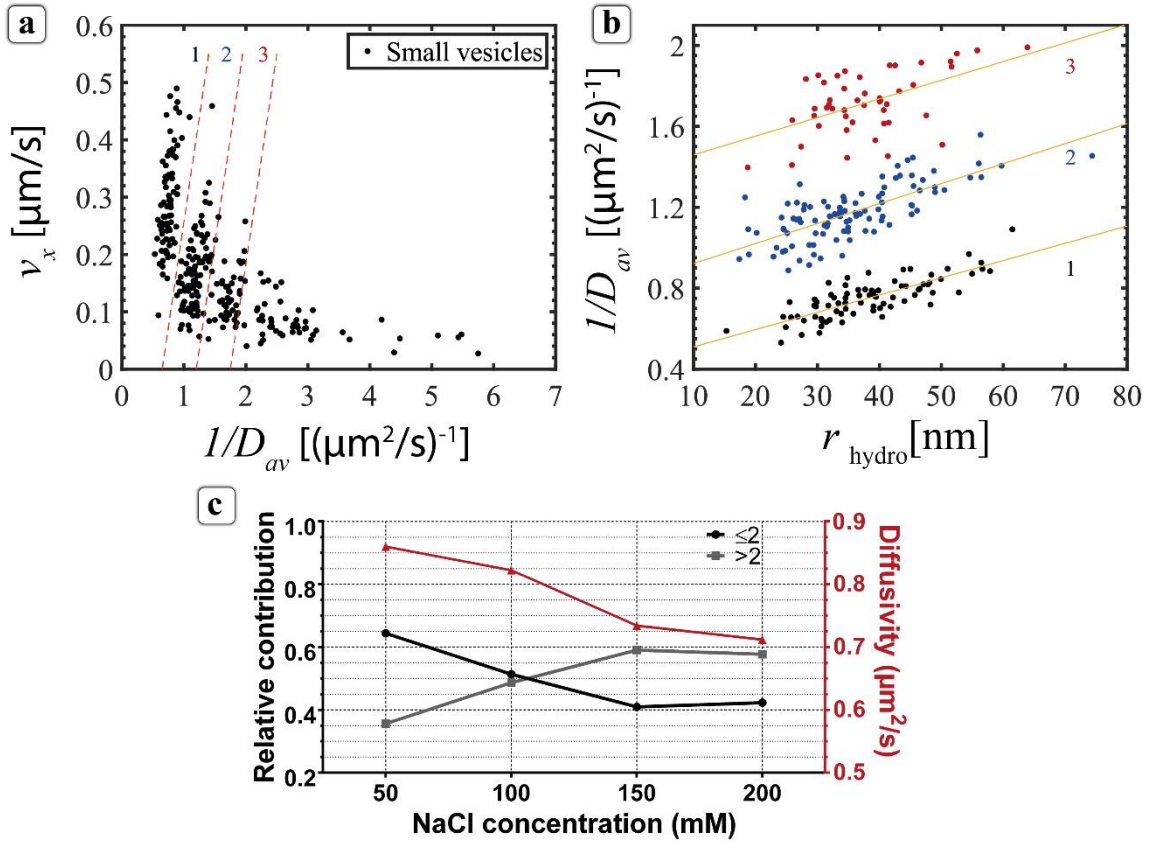

Figure 15. Flow-directional velocity versus inverse average diffusivity at 50 mM NaCl of (a) small unilamellar vesicles (SUVs), where the clustering, indicating differently tethered populations, is visible. The SUVs have on average 3 tethers per vesicle. The dashed red lines in (a) designate the selection based on the number of tethers (1, 2 and 3 respectively). (b) Inverse average diffusivity versus the hydrodynamic radius for SUVs based on each selection. The intercepts correspond to the diffusivity of the tethers without the contribution of the SUV. The linear fits (orange) are the following: 1-tether: $D_{av}^{-1} = 0.009 r_{hydro} + 0.42$; 2-tether: $D_{av}^{-1} = 0.010 r_{hydro} + 0.82$; 3-tether: $D_{av}^{-1} = 0.009 r_{hydro} + 1.37$. (c) Relative frequency of few (≤2) and many (>2) tethers versus external salt concentration showing that the average amount of tethers per vesicle increases with increasing salt. The average diffusivity (red) decreases with increasing salt concentration.

5 Future outlook

In addition to the papers included in the thesis, there are several prospective projects furthering nanoparticle characterization, which will be discussed below.

5.1 Determination of BNP concentration

To compliment the information about the size, molecular content and structure obtained by using the techniques described in this thesis, it is also crucial to quantify the concentration of BNPs. The BNP concentration can be central for medical applications, for example, it is believed that the concentration of specific EVs, e.g., exosomes, is altered for patients affected with certain diseases [190]. Recently, Rupert et al. used surface plasmon resonance spectroscopy to determine exosome concentration in solution from the rate of exosome binding under diffusion limited conditions [191]. We planned to further this research by measuring both the rate binding of individual vesicles to an SLB combined with the 2DFN approach described in section 3.3.2 and Papers IV and V. The adsorption kinetics of vesicles can be investigated by directly measuring the rate of binding to a surface or to an SLB via tethering-chemistry. The rate of adsorption to the surface can follow two pathways: (i) reaction-limited binding, where the binding kinetics is determined by the actual binding to the surface or (ii) diffusion-limited binding, where the binding to the surface is so fast that the rate of binding is controlled by diffusion across a depletion zone near the surface. For rectangular flow geometry, the mass transfer to the surface can be characterized by the mass-transport coefficient [192,193]:

$$k_M = 0.98\left(\frac{D_i}{h}\right)^{\frac{2}{3}}\left(\frac{Q}{wl}\right)^{\frac{1}{3}}, \qquad 5.1.1$$

where D_i is the diffusion coefficient of the vesicle population with size i, Q the volumetric flow rate, and h, w, l are the height, width, and length of the channel, respectively. The rate of binding is then proportional to the analyte concentration according to [170,194]:

$$\frac{\Gamma_i}{\Delta t} = k_M C_i\,, \qquad 5.1.2$$

where $\Gamma_i/\Delta t$ is the rate of binding per surface area of vesicle subpopulation with size i and C_i is the concentration of the corresponding subpopulation. However, the adsorption rate to the surface under flow conditions may differ at various points on the surface, depending on the distance from the inlet to the measurement area [170]. Therefore, we designed a PDMS chip (Figure 16a) to minimize effects from depletion and buildup of a depletion layer, which can be caused due to liquid passage between the measurement area and the sample container. In order

to test the PDMS chip design, we measured several time series of Rhodamine-labelled POPC vesicles binding to the glass floor of a microfluidic chip. Figure 16b shows two binding experiments with the same flow rate, but in different regions of the PDMS chip. The higher rate of binding was observed in the second region of the channel, which consequently lead to differences in the concentration estimation. The concentration was calculated according to eq. 5.1.2 and compared to the concentration value estimated from the molar concentration of vesicles in the prepared solution determined the total amount of lipids and their size distribution according to NTA data. While comparing these two values, an agreement better than >90% (out of >10 experiments) was obtained for the data recorded in the second region of the channel. In principle, this result suggested that the chip design was suitable for further experiments.

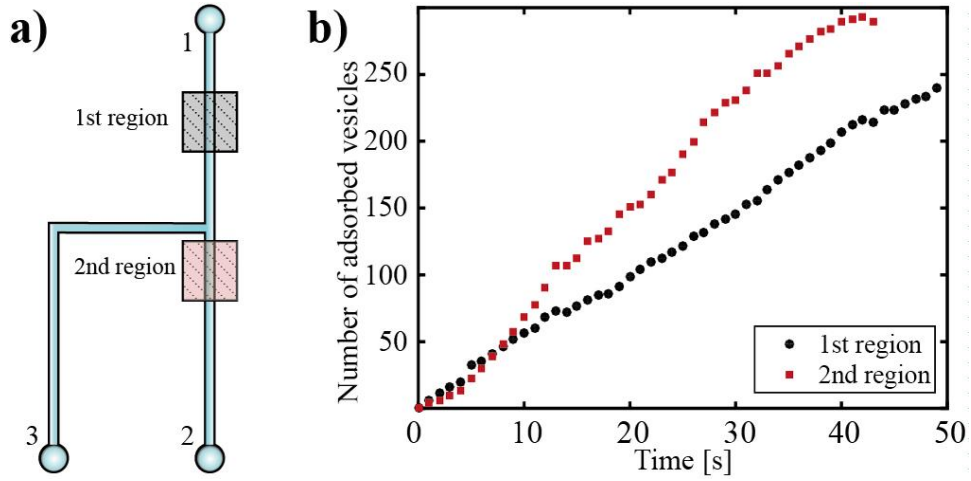

Figure 16. Microfluidic flow chamber specifics (a) Schematic of the channel geometry. Two equal flows of the sample from inlet 1, and buffer from inlet 2, are introduced simultaneously, whereas 3 acts as an outlet. During this introduction, a fluorescent time series of images is taken in the 1st region. Following this, outlet 3 is closed, and inlet 2 is opened, while the sample is still being introduced from inlet 1. Another time series is taken in the 2nd region. (b) Number of detected vesicles within the 1st (black dots) and 2nd (red squares) regions of the channel plotted versus time, for a 100 × 100 μm^2 surface area.

This approach can in principle be extended to BNP binding to an SLB. However, it remains difficult to combine both the size and concentration determination in one experiment, to in that way determine both the concentration of differently sized particle sub-populations and molecular content. To ensure mass-transport limited conditions, a high-affinity binding chemistry such as neutravidin-biotin is needed. However, particles tethered in this way are not easy to shear with a hydrodynamic flow. Another option is to continue with DNA-tethering, with mobile vesicles as was done in 2DFN. However, this might switch the rate of binding to the reaction-limited regime, which will require calibration data in which the reaction kinetics is verified. Alternatively, as the 2DFN method can be used to determine if a specific BNP-dye

combination incorporates proportionally to particle size (Paper IV), this approach could be combined with the concentration determination of BNPs obtained from the rate by which they bind to the surface. In this way, one could in principle determine both the concentration and individual size of complex BNP sub-populations. In either case, this would enable for the method to become more multi-parametric, by enabling size, concentration and molecular content determinations – all in one experiment.

5.2 Native drug-delivery vehicles

Since drug delivery vehicles made of synthetic lipids encounter a multitude of limitations for *in vivo* applications, much interest has been focused on harnessing BNPs for drug-delivery applications [195]. For example, limitations such as poor uptake and non-specific drug release can potentially be overcome by using NMVs (more thoroughly discussed in section 1.4.3), which are obtained via mechanical cell lysis [100], or exosomes [196]. Compared to synthetic vesicles, NMVs have high biocompatibility, long retention time *in vivo* and efficient cellular uptake [197]. Further, NMVs can be combined with mesoporous silica nanoparticles (MSNs) which have several beneficial properties – tunable size, high stability, high biocompatibility, high drug loading, and controlled drug release [79]. In future work, we will explore this possibility by sonicating NMVs together with MSNs, similarly to how synthetic vesicles were previously used for the same purpose [198]. To validate if the MSNs are lipid coated, both membrane dyes and TEM will be used (having uncoated bare particles as the control) [199]. If protocols can be found to ensure the encapsulation of MSNs was effective, we plan to determine if cellular uptake of native MSNs is increased *in vivo*, compared to non-native protocells.

5.3 Multiplexed characterization of biological nanoparticles under flow

BNPs like viruses and EVs commonly serve as carriers of various bioactive cargo, such as mRNA, DNA and proteins protected by the membrane envelope. In Paper IV we found that the complex membranes of NMVs and EVs affect incorporation efficiency of linkers and dye labels. Membrane composition and morphology is instrumental for the biological function of BNPs as membrane-membrane interactions will define the entry, or absence thereof, of the BNPs in a given cell. However, the final biological effect, whether beneficial or hazardous, will be determined by the interaction of the contents of the BNPs with the cell machinery. Thus, it is of relevance to precisely determine the content within BNPs and identify their sub-populations in size using 2DFN. One instructive illustration of the significance of such

investigations is that for viruses such as influenza A and HSV-1, only a small sub-population of the whole virus population is infectious and it is currently very challenging to ascertain which parameters differentiate the harmful viruses from the inert ones [200–202]. Furthermore, for BNPs, depending exclusively on labeling restricts the analysis to components which can be efficiently labelled and may also perturb the function of the particle. To overcome these potential limitations, but still benefit from chemical recognition given by fluorophore labels, a combined TIRF and interferometric scattering microscopy (iSCAT) approach may be used [203]. iSCAT does not rely on efficient dye incorporation since it is a label-free technique where the signal is based on interferometric scattering [203]. This signal is related to the dry mass of the BNP, which in turn, can be used to estimate the amount of cargo inside the BNP [204]. Furthermore, the combined information about size and iSCAT signal could potentially be used to quantify both size and effective refractive index on a single-particle level. Nevertheless, the complimentary fluorescence signal can still be used to label the BNP itself. The multiplexed nature of the technique could also be used to measure and thus differentiate between sub-populations of different EVs or separate viruses with and without cargo. This combined approach could also solve the potential issue of encapsulation efficiency in the prospective NMV-coated MSNs approach by using membrane-dyes in the native lipid membrane while observing whether the NPs are indeed loaded with MSNs by monitoring their scattering signal with iSCAT.

5.4 Viruses and two-dimensional flow nanometry

Many membrane-enveloped viruses, for instance HSV-1, are known to attach to the membrane of the host cell and diffuse through a rather large region of the membrane surface before entering the cell through fusion between its viral envelope and the plasma membrane, whereby the host cell is usually killed in the viral replication process [205]. Attachment of various viruses is mediated by specific glycoproteins on the surface of the virus, which bind to receptors/sugar molecules on the cell surface [206], facilitating transmission of virus between the host cells. Since the viral entry is mediated by membrane fusion through the binding of protein ligands to cell-surface receptors, this opens up a possibility to monitor virus binding to cell membrane mimics (see section 1.3) and the mobility of the virus on the surface using advanced surface-based characterization techniques, such as 2DFN, that can effectively monitor this process. A better understanding of the virus-membrane interaction could help develop new drugs that inhibit the binding/mobility of the viral particle and therefore stop the infection in the early stage. In addition, such experiments may shed light on differentiating two

sub-populations as mentioned above. It might be the case that the virus particles in the non-infectious sub-population have all the genetic material and proteins needed for a successful infection, but, due to some defect, lack the capabilities for entering the cell efficiently. As described in previous chapters 2DFN can simultaneously access size and composition (via targeted protein or membrane labelling) of BNPs. This will allow performing population studies in virus samples, which can be compared with independent infective tests such as the well-established plaque assay. Even though, it was evident from the results presented in Paper IV that the incorporation of cholesterol-DNA as well as labelling was affected in case of native BNPs, preliminary experiments have already demonstrated that, from the point of view of labelling and cholesterol-DNA tethering to an SLB, 2DFN can be successfully applied to HSV-1 as well.

5.5 High-throughput size determination

Since incorporation efficiency of DNA-linkers is dependent on the membrane of the BNP as inferred from Paper IV or even impossible in the case of BNPs without a membrane envelope, it is crucial to find means to carry out similar measurements in bulk. Contrarily to ordinary 2DFN, it is possible to confine individual particles in high-aspect ratio nanochannels of 300 nm in both width and height, but several millimeters in length. Since the particles are of similar size as the channel cross-section, they will be unable to diffuse perpendicularly to the flow direction. In the flow direction they will experience hindered diffusion and thus a similar correction factor as presented in eq. 3.3.19 can be used together with the contribution from all channel walls [207]. In this way, the size of BNPs can be estimated from their flow-directional diffusivity by taking appropriate corrections into account. Furthermore, as these NPs stay within the focal plane, the intensity determination will be similar to the 2DFN case, which consequently enables the simultaneous determination of size and intensity of different BNPs in a high-throughput manner. Figure 17 shows the measurement set up and a dataset with Rhodamine-labelled vesicles, depicting a size distribution of these particles. Furthermore, the size distribution in this case does not need adjustment or calibration, as the size of each BNP is calculated directly from their diffusivity according to equation 3.3.8 by taking into account the effect of the walls [207], illustrating the applicability of this method for non-tethered nanometer-scale biological systems. The development of this nanofluidic platform is currently in progress and has been used to distinguish complex size distributions, determine size and colocalize individual particles while maintaining a high throughput [208].

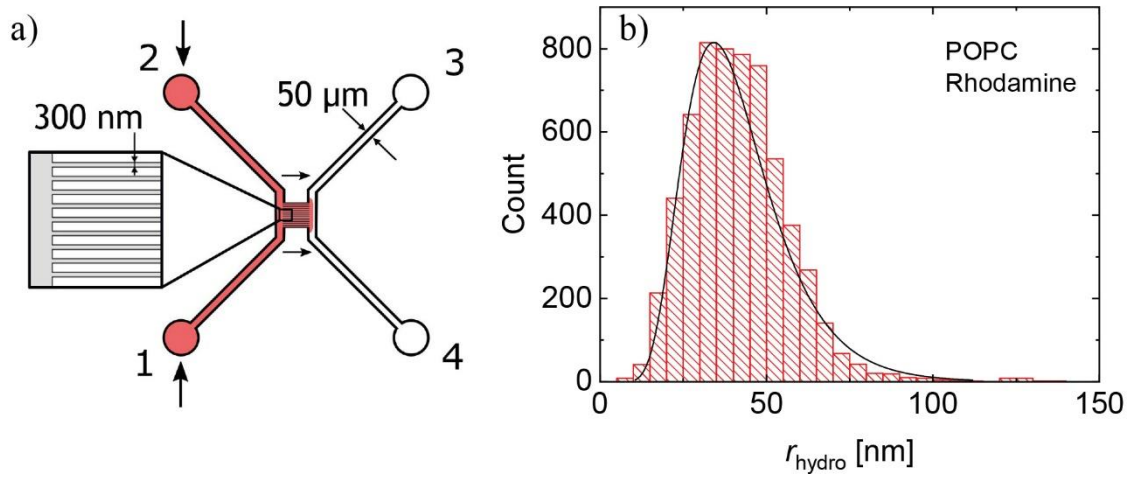

Figure 17. Analysis of Rhodamine-labelled vesicles (a) Measurement setup, where two equal flows of the sample from inlet 1 and inlet 2 are introduced into the 300 nm width and height nanochannels, where the fluorescence time series is taken. 3 and 4 are the outlets. (b) size distribution with a log-normal fit (line) determined using the hindered diffusion model.

6 Acknowledgements

The past several years have been an amazing journey through which I have experienced so many different cultures and met many wonderful people from different parts of the globe. The following people have left the most profound impact on me during my approximately 4.5 years as a PhD student, to whom my sincere gratitude and appreciation is due.

First of all, I would like to thank my supervisors *Fredrik Höök, Gavin Jeffries and Paul Joyce*, for your wise words, guidance and support throughout my PhD journey. *Fredrik*, my main supervisor, you have encouraged and inspired me numerous times and I am in awe of your visionary thought-processes. Furthermore, I am grateful that you suggested me to start teaching already at the start of my PhD – as a result have met many bright minds of which some have even joined our group. I thank you for giving me this opportunity to challenge myself in a broader capacity! *Gavin*, on the other hand, you are a guru of all-things technology, the go-to guy who knows quite a fair bit about everything, especially microscopy and data analysis. Thank you for guiding and co-supervising me even after leaving academia! *Paul*, however, you've kept my feet on the ground while doing experiments in the lab and have made me gather and organize my thoughts successfully, and helped to actually put them on paper. Thank you, mate!

The following people have made a major impact in my professional life, either by giving me valuable advice in the lab or otherwise helping me – *Quentin*, *Mokhtar*, *Björn, son of Agnar*, *Erik* and *Adrián*. Furthermore, this thesis would probably look quite a bit different if it weren't for the ongoing suggestions from *you* in addition to my supervisors. Of course, I have not forgotten all the past and current members of the *Biological Physics Group* and all my previous officemates next to the kitchen – *Mokhtar, Irem, Iwan* to mention a few and my current officemate *Christoffer,* who have accelerated these crazy discussions and otherwise made my work (and after-work) life enjoyable. Thank you! It has been an honor to meet all these awesome people at Chalmers.

I thank the following people for proof-reading parts of this thesis and otherwise supporting me: *Adrián*, *Erik*, *Björn*, *Felix*, *Ilja*, *Justas*, *Alvaro*, *Sandra* and *Margit*.

There are also some people, who have left Chalmers during this time whom I dearly miss – *Hudson*, *Marta*, *Olov*, *Nagma, Nadia, Juliane, Deborah, Hoda* and *Thomas*. A special shout-out goes to *Kiryl*, who was my first friend in Sweden and *Bella*, my first Swedish friend. I am also grateful to *Aldo* and *Alar* for taking me under your wing when I first came to Sweden and my Estonian mentor *Alvo* for supporting my efforts to come to Sweden and *Inga* for showing me that its possible in the 1st place!

I would also like to acknowledge all my co-authors that contributed to my publications.

Thank you, *Margit*, for supporting me throughout this journey and drawing the cute BNPs in the key chapters of the thesis!

I am truly grateful for all my friends here, in Estonia and all around the world. People really do make the journey!

Viimaks tänan ma südamest oma kallist ema, kes on mulle alati parimat soovinud ja mind alati toetanud, ükstapuha, mis valiku ees ma seisaks. See on kindel, et pealehakkamise (minu puhul põikpäisuse) olen saanud sinult! ☺

Like Gollum said, some things really are 'My precious!'

References

[1] M. Prince, A. Comas-Herrera, M. Knapp, M. Guerchet, M. Karagiannidou, World Alzheimer Report 2016 Improving healthcare for people living with dementia. Coverage, Quality and costs now and in the future, Alzheimer's Dis. Int. (2016) 1–140. https://doi.org/10.13140/RG.2.2.22580.04483.

[2] K.M. Candelario, D. a Steindler, The role of extracellular vesicles in the progression of neurodegenerative disease and cancer., Trends Mol. Med. 20 (2014) 368–74. https://doi.org/10.1016/j.molmed.2014.04.003.

[3] G. Raposo, W. Stoorvogel, Extracellular vesicles: Exosomes, microvesicles, and friends, J. Cell Biol. 200 (2013) 373–383. https://doi.org/10.1083/jcb.201211138.

[4] R. Xu, D.W. Greening, H.-J. Zhu, N. Takahashi, R.J. Simpson, Extracellular vesicle isolation and characterization: toward clinical application, J. Clin. Invest. 126 (2016) 1152–1162. https://doi.org/10.1172/JCI81129.

[5] J. De Toro, L. Herschlik, C. Waldner, C. Mongini, Emerging Roles of Exosomes in Normal and Pathological Conditions: New Insights for Diagnosis and Therapeutic Applications, Front. Immunol. 6 (2015) 1–12. https://doi.org/10.3389/fimmu.2015.00203.

[6] S. El Andaloussi, I. Mäger, X.O. Breakefield, M.J.A. Wood, Extracellular vesicles: Biology and emerging therapeutic opportunities, Nat. Rev. Drug Discov. 12 (2013) 347–357. https://doi.org/10.1038/nrd3978.

[7] M.W. Tibbitt, J.E. Dahlman, R. Langer, Emerging Frontiers in Drug Delivery, J. Am. Chem. Soc. 138 (2016) 704–717. https://doi.org/10.1021/jacs.5b09974.

[8] C. Quek, A.F. Hill, The role of extracellular vesicles in neurodegenerative diseases, Biochem. Biophys. Res. Commun. 483 (2017) 1178–1186. https://doi.org/10.1016/j.bbrc.2016.09.090.

[9] L. Zhu, K. Wang, J. Cui, H. Liu, X. Bu, H. Ma, W. Wang, H. Gong, C. Lausted, L. Hood, et al., Label-Free Quantitative Detection of Tumor-Derived Exosomes through Surface Plasmon Resonance Imaging, Anal. Chem. 86 (2014) 8857–8864. https://doi.org/10.1021/ac5023056.

[10] R. Bello-Morales, B. Praena, C. de la Nuez, M.T. Rejas, M. Guerra, M. Galán, M. Izquierdo, V. Calvo, C. Krummenacher, J.A. López-Guerrero, Role of microvesicles in the spread of Herpes simplex virus type 1 in oligodendrocytic cells, J. Virol. 92 (2018) JVI.00088-18. https://doi.org/10.1128/JVI.00088-18.

[11] M. Santiana, S. Ghosh, B.A. Ho, V. Rajasekaran, W.-L. Du, Y. Mutsafi, D.A. De Jésus-Diaz, S. V. Sosnovtsev, E.A. Levenson, G.I. Parra, et al., Vesicle-Cloaked Virus Clusters Are Optimal Units for Inter-organismal Viral Transmission, Cell Host Microbe. 24 (2018) 208-220.e8. https://doi.org/10.1016/j.chom.2018.07.006.

[12] B. György, T.G. Szabó, M. Pásztói, Z. Pál, P. Misják, B. Aradi, V. László, É. Pállinger, E. Pap, Á. Kittel, et al., Membrane vesicles, current state-of-the-art: emerging role of extracellular vesicles, Cell. Mol. Life Sci. 68 (2011) 2667–2688. https://doi.org/10.1007/s00018-011-0689-3.

[13] S. Block, B.J. Fast, A. Lundgren, V.P. Zhdanov, F. Höök, Two-dimensional flow nanometry of biological nanoparticles for accurate determination of their size and emission intensity, Nat. Commun. 7 (2016) 12956. https://doi.org/10.1038/ncomms12956.

[14] B. Alberts, A. Johnson, J. Lewis, M. Raff, K. Roberts, P. Walter, Molecular Biology of the Cell, Fifth Edition, Garland Publishing Inc., New York, NY, 2007.

[15] R.A.L. Jones, Soft condensed matter, Oxford University Press, 2003.

[16] D.B. Fenske, M.A. Monck, P.R. Cullis, M.J. Hope, The functional roles of lipids in

biological membranes, in: Biomembr. A Multi-Volume Treatise, 1995: pp. 1–28. https://doi.org/10.1016/S1874-5342(06)80053-X.
[17] E. Fahy, S. Subramaniam, H.A. Brown, C.K. Glass, A.H. Merrill, R.C. Murphy, C.R.H. Raetz, D.W. Russell, Y. Seyama, W. Shaw, et al., A comprehensive classification system for lipids, J. Lipid Res. 46 (2005) 839–862. https://doi.org/10.1194/jlr.E400004-JLR200.
[18] G. van Meer, D.R. Voelker, G.W. Feigenson, Membrane lipids: where they are and how they behave, Nat. Rev. Mol. Cell Biol. 9 (2008) 112–124. https://doi.org/10.1038/nrm2330.
[19] R.B. Gennis, Biomembranes: molecular structure and function, Springer New York, New York, NY, 1989. https://doi.org/10.1007/978-1-4757-2065-5.
[20] R. Breslow, Hydrophobic effects on simple organic reactions in water, Acc. Chem. Res. 24 (1991) 159–164. https://doi.org/10.1021/ar00006a001.
[21] Y.-H.M. Chan, S.G. Boxer, Model membrane systems and their applications., Curr. Opin. Chem. Biol. 11 (2007) 581–7. https://doi.org/10.1016/j.cbpa.2007.09.020.
[22] N. Jacob, N. Israelachvili, Intermolecular and Surface Forces, Elsevier, 2011. https://doi.org/10.1016/C2011-0-05119-0.
[23] C. Théry, L. Zitvogel, S. Amigorena, Exosomes: composition, biogenesis and function., Nat. Rev. Immunol. 2 (2002) 569–79. https://doi.org/10.1038/nri855.
[24] R.C. MacDonald, R.I. MacDonald, B.P. Menco, K. Takeshita, N.K. Subbarao, L.R. Hu, Small-volume extrusion apparatus for preparation of large, unilamellar vesicles., Biochim. Biophys. Acta. 1061 (1991) 297–303. https://doi.org/10.1016/0005-2736(91)90295-j.
[25] J.N. Israelachvili, S. Marcelja, R.G. Horn, Physical principles of membrane organization., Q. Rev. Biophys. 13 (1980) 121–200. https://doi.org/10.1017/S0033583500001645.
[26] A. Kunze, M. Bally, F. Höök, G. Larson, Equilibrium-fluctuation-analysis of single liposome binding events reveals how cholesterol and Ca2+ modulate glycosphingolipid trans-interactions, Sci. Rep. 3 (2013) 1452. https://doi.org/10.1038/srep01452.
[27] A.-S. Cans, N. Wittenberg, R. Karlsson, L. Sombers, M. Karlsson, O. Orwar, A. Ewing, Artificial cells: Unique insights into exocytosis using liposomes and lipid nanotubes, Proc. Natl. Acad. Sci. 100 (2003) 400–404. https://doi.org/10.1073/pnas.232702599.
[28] S.F. Fenz, K. Sengupta, Giant vesicles as cell models, Integr. Biol. 4 (2012) 982. https://doi.org/10.1039/c2ib00188h.
[29] B.C. Buddingh', J.C.M. Van Hest, Artificial Cells: Synthetic Compartments with Life-like Functionality and Adaptivity, Acc. Chem. Res. 50 (2017) 769–777. https://doi.org/10.1021/acs.accounts.6b00512.
[30] M. Zagnoni, Miniaturised technologies for the development of artificial lipid bilayer systems, Lab Chip. 12 (2012) 1026. https://doi.org/10.1039/c2lc20991h.
[31] R.C. Cammarata, Surface and interface stress effects in thin films, Prog. Surf. Sci. 46 (1994) 1–38. https://doi.org/10.1016/0079-6816(94)90005-1.
[32] R. Shuttleworth, The Surface Tension of Solids, Proc. Phys. Soc. Sect. A. 63 (1950) 444–457. https://doi.org/10.1088/0370-1298/63/5/302.
[33] T.S. Jakubov, D.E. Mainwaring, The surface tension of a solid at the solid–vacuum interface, an evaluation from adsorption and wall potential calculations, J. Colloid Interface Sci. 307 (2007) 477–480. https://doi.org/10.1016/j.jcis.2006.12.034.
[34] I. Czolkos, A. Jesorka, O. Orwar, Molecular phospholipid films on solid supports, Soft Matter. 7 (2011) 4562. https://doi.org/10.1039/c0sm01212b.
[35] V. Tandon, S.K. Bhagavatula, W.C. Nelson, B.J. Kirby, Zeta potential and electroosmotic mobility in microfluidic devices fabricated from hydrophobic polymers:

1. The origins of charge, Electrophoresis. 29 (2008) 1092–1101. https://doi.org/10.1002/elps.200700734.
[36] R. Zimmermann, S. Dukhin, C. Werner, Electrokinetic Measurements Reveal Interfacial Charge at Polymer Films Caused by Simple Electrolyte Ions, J. Phys. Chem. B. 105 (2001) 8544–8549. https://doi.org/10.1021/jp004051u.
[37] J.-P. Jolivet, M. Henry, J. Livage, E. Bescher, Metal oxide chemistry and synthesis: from solution to solid state, John Wiley New York, 2000.
[38] R.J. Hunter, Zeta Potential in Colloid Science, Elsevier, 1981. https://doi.org/10.1016/C2013-0-07389-6.
[39] J. Raedler, H. Strey, E. Sackmann, Phenomenology and Kinetics of Lipid Bilayer Spreading on Hydrophilic Surfaces, Langmuir. 11 (1995) 4539–4548. https://doi.org/10.1021/la00011a058.
[40] R.P. Richter, R. Bérat, A.R. Brisson, Formation of Solid-Supported Lipid Bilayers: An Integrated View, Langmuir. 22 (2006) 3497–3505. https://doi.org/10.1021/la052687c.
[41] A.P.G. Egrot, C.A. Marquette, L.J. Blum, Biomimetic membranes and biomolecule immobilisation strategies for nanobiotechnology applications, Int. J. Nanotechnol. 7 (2010) 753. https://doi.org/10.1504/IJNT.2010.031743.
[42] J. Nissen, S. Gritsch, G. Wiegand, J.O. Rädler, Wetting of phospholipid membranes on hydrophilic surfaces - Concepts towards self-healing membranes, Eur. Phys. J. B. 10 (1999) 335–344. https://doi.org/10.1007/s100510050862.
[43] I. Gözen, P. Dommersnes, I. Czolkos, A. Jesorka, T. Lobovkina, O. Orwar, Fractal avalanche ruptures in biological membranes, Nat. Mater. 9 (2010) 908–912. https://doi.org/10.1038/nmat2854.
[44] B. Sanii, A.N. Parikh, Surface-energy dependent spreading of lipid monolayers and bilayers, Soft Matter. 3 (2007) 974. https://doi.org/10.1039/b704827k.
[45] I. Czolkos, Y. Erkan, P. Dommersnes, A. Jesorka, O. Orwar, Controlled formation and mixing of two-dimensional fluids., Nano Lett. 7 (2007) 1980–4. https://doi.org/10.1021/nl070726u.
[46] P.S. Cremer, S.G. Boxer, Formation and Spreading of Lipid Bilayers on Planar Glass Supports, J. Phys. Chem. B. 103 (1999) 2554–2559. https://doi.org/10.1021/jp983996x.
[47] A.S. Muresan, K.Y.C. Lee, Shape Evolution of Lipid Bilayer Patches Adsorbed on Mica: an Atomic Force Microscopy Study, J. Phys. Chem. B. 105 (2001) 852–855. https://doi.org/10.1021/jp001813c.
[48] R.P. Richter, A.R. Brisson, Following the Formation of Supported Lipid Bilayers on Mica: A Study Combining AFM, QCM-D, and Ellipsometry, Biophys. J. 88 (2005) 3422–3433. https://doi.org/10.1529/biophysj.104.053728.
[49] E. Sackmann, Supported Membranes: Scientific and Practical Applications, Science (80-.). 271 (1996) 43–48. https://doi.org/10.1126/science.271.5245.43.
[50] B. Wolfrum, Y. Mourzina, F. Sommerhage, A. Offenhäusser, Suspended Nanoporous Membranes as Interfaces for Neuronal Biohybrid Systems, Nano Lett. 6 (2006) 453–457. https://doi.org/10.1021/nl052370x.
[51] F.F. Rossetti, M. Bally, R. Michel, M. Textor, I. Reviakine, Interactions between Titanium Dioxide and Phosphatidyl Serine-Containing Liposomes: Formation and Patterning of Supported Phospholipid Bilayers on the Surface of a Medically Relevant Material, Langmuir. 21 (2005) 6443–6450. https://doi.org/10.1021/la0509100.
[52] P.K. Ang, M. Jaiswal, C.H.Y.X. Lim, Y. Wang, J. Sankaran, A. Li, C.T. Lim, T. Wohland, Ö. Barbaros, K.P. Loh, A Bioelectronic Platform Using a Graphene−Lipid Bilayer Interface, ACS Nano. 4 (2010) 7387–7394. https://doi.org/10.1021/nn1022582.
[53] B.M. Blaschke, P. Böhm, S. Drieschner, B. Nickel, J.A. Garrido, Lipid Monolayer Formation and Lipid Exchange Monitored by a Graphene Field-Effect Transistor,

Langmuir. 34 (2018) 4224–4233. https://doi.org/10.1021/acs.langmuir.8b00162.
[54] S. Gritsch, P. Nollert, F. Jähnig, E. Sackmann, Impedance spectroscopy of porin and gramicidin pores reconstituted into supported lipid bilayers on indium-tin-oxide electrodes, Langmuir. 14 (1998) 3118–3125. https://doi.org/10.1021/la9710381.
[55] E. Moore, O. Rawley, T. Wood, P. Galvin, Monitoring of cell growth in vitro using biochips packaged with indium tin oxide sensors, Sensors Actuators, B Chem. 139 (2009) 187–193. https://doi.org/10.1016/j.snb.2008.11.025.
[56] A. Oliveros, A. Guiseppi-Elie, S.E. Saddow, Silicon carbide: a versatile material for biosensor applications, Biomed. Microdevices. 15 (2013) 353–368. https://doi.org/10.1007/s10544-013-9742-3.
[57] G. Bonaventura, R. Iemmolo, V. La Cognata, M. Zimbone, F. La Via, M.E. Fragalà, M.L. Barcellona, R. Pellitteri, S. Cavallaro, Biocompatibility between Silicon or Silicon Carbide surface and Neural Stem Cells, Sci. Rep. 9 (2019) 1–13. https://doi.org/10.1038/s41598-019-48041-3.
[58] L.K. Tamm, H.M. McConnell, Supported phospholipid bilayers., Biophys. J. 47 (1985) 105–13. https://doi.org/10.1016/S0006-3495(85)83882-0.
[59] S.J. Johnson, T.M. Bayerl, D.C. McDermott, G.W. Adam, A.R. Rennie, R.K. Thomas, E. Sackmann, Structure of an adsorbed dimyristoylphosphatidylcholine bilayer measured with specular reflection of neutrons, Biophys. J. 59 (1991) 289–294. https://doi.org/10.1016/S0006-3495(91)82222-6.
[60] E.T. Castellana, P.S. Cremer, Solid supported lipid bilayers: From biophysical studies to sensor design, Surf. Sci. Rep. 61 (2006) 429–444. https://doi.org/10.1016/j.surfrep.2006.06.001.
[61] H. Schönherr, J.M. Johnson, P. Lenz, C.W. Frank, S.G. Boxer, Vesicle Adsorption and Lipid Bilayer Formation on Glass Studied by Atomic Force Microscopy, Langmuir. 20 (2004) 11600–11606. https://doi.org/10.1021/la049302v.
[62] J.M. Johnson, T. Ha, S. Chu, S.G. Boxer, Early steps of supported bilayer formation probed by single vesicle fluorescence assays., Biophys. J. 83 (2002) 3371–9. https://doi.org/10.1016/S0006-3495(02)75337-X.
[63] C.A. Keller, K. Glasmästar, V.P. Zhdanov, B. Kasemo, Formation of Supported Membranes from Vesicles, Phys. Rev. Lett. 84 (2000) 5443–5446. https://doi.org/10.1103/PhysRevLett.84.5443.
[64] I. Gözen, A. Jesorka, Instrumental Methods to Characterize Molecular Phospholipid Films on Solid Supports, Anal. Chem. 84 (2012) 822–838. https://doi.org/10.1021/ac203126f.
[65] J. Salafsky, J.T. Groves, S.G. Boxer, Architecture and Function of Membrane Proteins in Planar Supported Bilayers : A Study with Photosynthetic Reaction Centers †, 2960 (1996) 14773–14781.
[66] K. Dimitrievski, B. Kasemo, Simulations of Lipid Vesicle Adsorption for Different Lipid Mixtures, Langmuir. 24 (2008) 4077–4091. https://doi.org/10.1021/la703021u.
[67] J. Ding, D.Y. Takamoto, a von Nahmen, M.M. Lipp, K.Y. Lee, a J. Waring, J. a Zasadzinski, Effects of lung surfactant proteins, SP-B and SP-C, and palmitic acid on monolayer stability., Biophys. J. 80 (2001) 2262–72. https://doi.org/10.1016/S0006-3495(01)76198-X.
[68] S. Baoukina, D.P. Tieleman, Lung surfactant protein SP-B promotes formation of bilayer reservoirs from monolayer and lipid transfer between the interface and subphase., Biophys. J. 100 (2011) 1678–87. https://doi.org/10.1016/j.bpj.2011.02.019.
[69] a. J. Bron, J.M. Tiffany, S.M. Gouveia, N. Yokoi, L.W. Voon, Functional aspects of the tear film lipid layer, Exp. Eye Res. 78 (2004) 347–360. https://doi.org/10.1016/j.exer.2003.09.019.

[70] P. Kulovesi, J. Telenius, A. Koivuniemi, G. Brezesinski, A. Rantamäki, T. Viitala, E. Puukilainen, M. Ritala, S.K. Wiedmer, I. Vattulainen, et al., Molecular organization of the tear fluid lipid layer., Biophys. J. 99 (2010) 2559–67. https://doi.org/10.1016/j.bpj.2010.08.001.
[71] J.F. Poduslo, K.L. Hultman, G.L. Curran, G.M. Preboske, R. Chamberlain, M. Marjańska, M. Garwood, C.R. Jack, T.M. Wengenack, Targeting Vascular Amyloid in Arterioles of Alzheimer Disease Transgenic Mice With Amyloid β Protein Antibody-Coated Nanoparticles, J. Neuropathol. Exp. Neurol. 70 (2011) 653–661. https://doi.org/10.1097/NEN.0b013e318225038c.
[72] Y. Gong, F.M. Winnik, Strategies in biomimetic surface engineering of nanoparticles for biomedical applications, Nanoscale. 4 (2012) 360–368. https://doi.org/10.1039/C1NR11297J.
[73] K.J. Seu, A.P. Pandey, F. Haque, E.A. Proctor, A.E. Ribbe, J.S. Hovis, Effect of Surface Treatment on Diffusion and Domain Formation in Supported Lipid Bilayers, Biophys. J. 92 (2007) 2445–2450. https://doi.org/10.1529/biophysj.106.099721.
[74] T. Charitat, E. Bellet-Amalric, G. Fragneto, F. Graner, Adsorbed and free lipid bilayers at the solid-liquid interface, Eur. Phys. J. B. 8 (1999) 583–593. https://doi.org/10.1007/s100510050725.
[75] S.R. Tabaei, J.-H. Choi, G. Haw Zan, V.P. Zhdanov, N.-J. Cho, Solvent-Assisted Lipid Bilayer Formation on Silicon Dioxide and Gold, Langmuir. 30 (2014) 10363–10373. https://doi.org/10.1021/la501534f.
[76] K. Sugihara, B. Jang, M. Schneider, J. Vörös, T. Zambelli, A universal method for planar lipid bilayer formation by freeze and thaw, Soft Matter. 8 (2012) 5525. https://doi.org/10.1039/c2sm25148e.
[77] A.A. Brian, H.M. Mcconnell, Allogeneic stimulation of cytotoxic T cells by supported planar membranes., Proc. Natl. Acad. Sci. U. S. A. 81 (1984) 6159–63. https://doi.org/10.1073/pnas.81.19.6159.
[78] E. Kalb, S. Frey, L.K. Tamm, Formation of supported planar bilayers by fusion of vesicles to supported phospholipid monolayers, Biochim. Biophys. Acta - Biomembr. 1103 (1992) 307–316. https://doi.org/10.1016/0005-2736(92)90101-Q.
[79] I. SLOWING, J. VIVEROESCOTO, C. WU, V. LIN, Mesoporous silica nanoparticles as controlled release drug delivery and gene transfection carriers☆, Adv. Drug Deliv. Rev. 60 (2008) 1278–1288. https://doi.org/10.1016/j.addr.2008.03.012.
[80] M. Hartmann, Ordered Mesoporous Materials for Bioadsorption and Biocatalysis, Chem. Mater. 17 (2005) 4577–4593. https://doi.org/10.1021/cm0485658.
[81] S. Angelos, M. Liong, E. Choi, J.I. Zink, Mesoporous silicate materials as substrates for molecular machines and drug delivery, Chem. Eng. J. 137 (2008) 4–13. https://doi.org/10.1016/j.cej.2007.07.074.
[82] S. Isaksson, E.B. Watkins, K.L. Browning, T. Kjellerup Lind, M. Cárdenas, K. Hedfalk, F. Höök, M. Andersson, Protein-Containing Lipid Bilayers Intercalated with Size-Matched Mesoporous Silica Thin Films, Nano Lett. 17 (2017) 476–485. https://doi.org/10.1021/acs.nanolett.6b04493.
[83] J. Rouquerol, D. Avnir, C.W. Fairbridge, D.H. Everett, J.M. Haynes, N. Pernicone, J.D.F. Ramsay, K.S.W. Sing, K.K. Unger, Recommendations for the characterization of porous solids (Technical Report), Pure Appl. Chem. 66 (1994) 1739–1758. https://doi.org/10.1351/pac199466081739.
[84] C.T. Kresge, M.E. Leonowicz, W.J. Roth, J.C. Vartuli, J.S. Beck, Ordered mesoporous molecular sieves synthesized by a liquid-crystal template mechanism, Nature. 359 (1992) 710–712. https://doi.org/10.1038/359710a0.
[85] D. Zhao, J. Feng, Q. Huo, N. Melosh, G.H. Fredrickson, B.F. Chmelka, G.D. Stucky,

Triblock Copolymer Syntheses of Mesoporous Silica with Periodic 50 to 300 Angstrom Pores, Science (80-.). 279 (1998) 548–552. https://doi.org/10.1126/science.279.5350.548.
[86] C.J. Brinker, Y. Lu, A. Sellinger, H. Fan, Evaporation-Induced Self-Assembly: Nanostructures Made Easy, Adv. Mater. 11 (1999) 579–585. https://doi.org/10.1002/(SICI)1521-4095(199905)11:7<579::AID-ADMA579>3.0.CO;2-R.
[87] M. Bally, K. Bailey, K. Sugihara, D. Grieshaber, J. Vörös, B. Städler, Liposome and Lipid Bilayer Arrays Towards Biosensing Applications, Small. 6 (2010) 2481–2497. https://doi.org/10.1002/smll.201000644.
[88] P. Weber, D. Ohlendorf, J. Wendoloski, F. Salemme, Structural origins of high-affinity biotin binding to streptavidin, Science (80-.). 243 (1989) 85–88. https://doi.org/10.1126/science.2911722.
[89] S. Svedhem, I. Pfeiffer, C. Larsson, C. Wingren, C. Borrebaeck, F. Höök, Patterns of DNA-Labeled and scFv-Antibody-Carrying Lipid Vesicles Directed by Material-Specific Immobilization of DNA and Supported Lipid Bilayer Formation on an Au/SiO2 Template, ChemBioChem. 4 (2003) 339–343. https://doi.org/10.1002/cbic.200390055.
[90] I. Pfeiffer, F. Höök, Bivalent Cholesterol-Based Coupling of Oligonucletides to Lipid Membrane Assemblies, J. Am. Chem. Soc. 126 (2004) 10224–10225. https://doi.org/10.1021/ja048514b.
[91] J.J. Benkoski, F. Höök, Lateral Mobility of Tethered Vesicle−DNA Assemblies, J. Phys. Chem. B. 109 (2005) 9773–9779. https://doi.org/10.1021/jp044947p.
[92] J. Carter, V.A. Saunders, Virology: principles and applications, John Wiley & Sons, 2007.
[93] P.S. Moore, Y. Chang, Why do viruses cause cancer? Highlights of the first century of human tumour virology, Nat. Rev. Cancer. 10 (2010) 878–889. https://doi.org/10.1038/nrc2961.
[94] K.J. Looker, A.S. Magaret, M.T. May, K.M.E. Turner, P. Vickerman, S.L. Gottlieb, L.M. Newman, Global and regional estimates of prevalent and incident herpes simplex virus type 1 infections in 2012, PLoS One. 10 (2015) 1–17. https://doi.org/10.1371/journal.pone.0140765.
[95] M. Yáñez-Mó, P.R.M. Siljander, Z. Andreu, A. Bedina Zavec, F.E. Borràs, E.I. Buzas, K. Buzas, E. Casal, F. Cappello, J. Carvalho, et al., Biological properties of extracellular vesicles and their physiological functions, J. Extracell. Vesicles. 4 (2015) 27066. https://doi.org/10.3402/jev.v4.27066.
[96] D. Maiolo, L. Paolini, G. Di Noto, A. Zendrini, D. Berti, P. Bergese, D. Ricotta, Colorimetric Nanoplasmonic Assay To Determine Purity and Titrate Extracellular Vesicles, Anal. Chem. 87 (2015) 4168–4176. https://doi.org/10.1021/ac504861d.
[97] S. Pant, H. Hilton, M.E. Burczynski, The multifaceted exosome: Biogenesis, role in normal and aberrant cellular function, and frontiers for pharmacological and biomarker opportunities, Biochem. Pharmacol. 83 (2012) 1484–1494. https://doi.org/10.1016/j.bcp.2011.12.037.
[98] H. Valadi, K. Ekström, A. Bossios, M. Sjöstrand, J.J. Lee, J.O. Lötvall, Exosome-mediated transfer of mRNAs and microRNAs is a novel mechanism of genetic exchange between cells, Nat. Cell Biol. 9 (2007) 654–659. https://doi.org/10.1038/ncb1596.
[99] L. Barile, G. Vassalli, Exosomes: Therapy delivery tools and biomarkers of diseases, Pharmacol. Ther. 174 (2017) 63–78. https://doi.org/10.1016/j.pharmthera.2017.02.020.
[100] H. Pace, L. Simonsson Nyström, A. Gunnarsson, E. Eck, C. Monson, S. Geschwindner, A. Snijder, F. Höök, Preserved Transmembrane Protein Mobility in Polymer-Supported Lipid Bilayers Derived from Cell Membranes, Anal. Chem. 87 (2015) 9194–9203.

https://doi.org/10.1021/acs.analchem.5b01449.
[101] C.E. Dodd, B.R.G. Johnson, L.J.C. Jeuken, T.D.H. Bugg, R.J. Bushby, S.D. Evans, Native E. coli inner membrane incorporation in solid-supported lipid bilayer membranes, Biointerphases. 3 (2008) FA59–FA67. https://doi.org/10.1116/1.2896113.
[102] E. Van Der Pol, A.G. Hoekstra, A. Sturk, C. Otto, T.G. Van Leeuwen, R. Nieuwland, Optical and non-optical methods for detection and characterization of microparticles and exosomes, J. Thromb. Haemost. 8 (2010) 2596–2607. https://doi.org/10.1111/j.1538-7836.2010.04074.x.
[103] M. Adrian, J. Dubochet, J. Lepault, A.W. McDowall, Cryo-electron microscopy of viruses, Nature. 308 (1984) 32–36. https://doi.org/10.1038/308032a0.
[104] C.J. Russo, S. Scotcher, M. Kyte, A precision cryostat design for manual and semi-automated cryo-plunge instruments, Rev. Sci. Instrum. 87 (2016) 114302. https://doi.org/10.1063/1.4967864.
[105] J. Dubochet, M. Adrian, J.-J. Chang, J.-C. Homo, J. Lepault, A.W. McDowall, P. Schultz, Cryo-electron microscopy of vitrified specimens, Q. Rev. Biophys. 21 (1988) 129–228.
[106] M. Almgren, K. Edwards, G. Karlsson, Cryo transmission electron microscopy of liposomes and related structures, Colloids Surfaces A Physicochem. Eng. Asp. 174 (2000) 3–21. https://doi.org/10.1016/S0927-7757(00)00516-1.
[107] Y. Yuana, R.I. Koning, M.E. Kuil, P.C.N. Rensen, A.J. Koster, R.M. Bertina, S. Osanto, Cryo-electron microscopy of extracellular vesicles in fresh plasma, J. Extracell. Vesicles. 2 (2013) 21494. https://doi.org/10.3402/jev.v2i0.21494.
[108] N. Arraud, R. Linares, S. Tan, C. Gounou, J.-M. Pasquet, S. Mornet, A.R. Brisson, Extracellular vesicles from blood plasma: determination of their morphology, size, phenotype and concentration, J. Thromb. Haemost. 12 (2014) 614–627. https://doi.org/10.1111/jth.12554.
[109] U. Erdbrügger, J. Lannigan, Analytical challenges of extracellular vesicle detection: A comparison of different techniques, Cytom. Part A. 89 (2016) 123–134. https://doi.org/10.1002/cyto.a.22795.
[110] R.F. Thompson, M. Walker, C.A. Siebert, S.P. Muench, N.A. Ranson, An introduction to sample preparation and imaging by cryo-electron microscopy for structural biology, Methods. 100 (2016) 3–15. https://doi.org/10.1016/j.ymeth.2016.02.017.
[111] G. Binnig, C.F. Quate, C. Gerber, Atomic Force Microscope, Phys. Rev. Lett. 56 (1986) 930–933. https://doi.org/10.1103/PhysRevLett.56.930.
[112] Y. YUANA, T.H. OOSTERKAMP, S. BAHATYROVA, B. ASHCROFT, P. GARCIA RODRIGUEZ, R.M. BERTINA, S. OSANTO, Atomic force microscopy: a novel approach to the detection of nanosized blood microparticles, J. Thromb. Haemost. 8 (2010) 315–323. https://doi.org/10.1111/j.1538-7836.2009.03654.x.
[113] S. Sharma, H.I. Rasool, V. Palanisamy, C. Mathisen, M. Schmidt, D.T. Wong, J.K. Gimzewski, Structural-Mechanical Characterization of Nanoparticle Exosomes in Human Saliva, Using Correlative AFM, FESEM, and Force Spectroscopy, ACS Nano. 4 (2010) 1921–1926. https://doi.org/10.1021/nn901824n.
[114] C. Gardiner, D. Di Vizio, S. Sahoo, C. Théry, K.W. Witwer, M. Wauben, A.F. Hill, Techniques used for the isolation and characterization of extracellular vesicles: Results of a worldwide survey, J. Extracell. Vesicles. 5 (2016). https://doi.org/10.3402/jev.v5.32945.
[115] A. Adan, G. Alizada, Y. Kiraz, Y. Baran, A. Nalbant, Flow cytometry: basic principles and applications, Crit. Rev. Biotechnol. 37 (2017) 163–176. https://doi.org/10.3109/07388551.2015.1128876.
[116] V. Shpacovitch, R. Hergenröder, Optical and surface plasmonic approaches to

characterize extracellular vesicles. A review, Anal. Chim. Acta. 1005 (2018) 1–15. https://doi.org/10.1016/j.aca.2017.11.066.
[117] E. van der Pol, F.A.W. Coumans, A.E. Grootemaat, C. Gardiner, I.L. Sargent, P. Harrison, A. Sturk, T.G. van Leeuwen, R. Nieuwland, Particle size distribution of exosomes and microvesicles determined by transmission electron microscopy, flow cytometry, nanoparticle tracking analysis, and resistive pulse sensing, J. Thromb. Haemost. 12 (2014) 1182–1192. https://doi.org/10.1111/jth.12602.
[118] A. Görgens, M. Bremer, R. Ferrer-Tur, F. Murke, T. Tertel, P.A. Horn, S. Thalmann, J.A. Welsh, C. Probst, C. Guerin, et al., Optimisation of imaging flow cytometry for the analysis of single extracellular vesicles by using fluorescence-tagged vesicles as biological reference material, J. Extracell. Vesicles. 8 (2019) 1587567. https://doi.org/10.1080/20013078.2019.1587567.
[119] N.A. Clark, J.H. Lunacek, G.B. Benedek, A Study of Brownian Motion Using Light Scattering, Am. J. Phys. 38 (1970) 575–585. https://doi.org/10.1119/1.1976408.
[120] J. Stetefeld, S.A. McKenna, T.R. Patel, Dynamic light scattering: a practical guide and applications in biomedical sciences, Biophys. Rev. 8 (2016) 409–427. https://doi.org/10.1007/s12551-016-0218-6.
[121] M. Kaszuba, D. McKnight, M.T. Connah, F.K. McNeil-Watson, U. Nobbmann, Measuring sub nanometre sizes using dynamic light scattering, J. Nanoparticle Res. 10 (2008) 823–829. https://doi.org/10.1007/s11051-007-9317-4.
[122] Z. Szakács, T. Mészáros, M.I. de Jonge, R.E. Gyurcsányi, Selective counting and sizing of single virus particles using fluorescent aptamer-based nanoparticle tracking analysis, Nanoscale. 10 (2018) 13942–13948. https://doi.org/10.1039/C8NR01310A.
[123] R.A. Dragovic, C. Gardiner, A.S. Brooks, D.S. Tannetta, D.J.P. Ferguson, P. Hole, B. Carr, C.W.G. Redman, A.L. Harris, P.J. Dobson, et al., Sizing and phenotyping of cellular vesicles using Nanoparticle Tracking Analysis, Nanomedicine Nanotechnology, Biol. Med. 7 (2011) 780–788. https://doi.org/10.1016/j.nano.2011.04.003.
[124] R. Carr, Optical detection and analysis of sub-micron particles, US6280960B1, 2001.
[125] E. Weatherall, G.R. Willmott, Applications of tunable resistive pulse sensing, Analyst. 140 (2015) 3318–3334. https://doi.org/10.1039/c4an02270j.
[126] E.C. Yusko, B.R. Bruhn, O.M. Eggenberger, J. Houghtaling, R.C. Rollings, N.C. Walsh, S. Nandivada, M. Pindrus, A.R. Hall, D. Sept, et al., Real-time shape approximation and fingerprinting of single proteins using a nanopore, Nat. Nanotechnol. 12 (2017) 360–367. https://doi.org/10.1038/nnano.2016.267.
[127] D. Branton, D.W. Deamer, A. Marziali, H. Bayley, S.A. Benner, T. Butler, M. Di Ventra, S. Garaj, A. Hibbs, X. Huang, et al., The potential and challenges of nanopore sequencing, Nat. Biotechnol. 26 (2008) 1146–1153. https://doi.org/10.1038/nbt.1495.
[128] J.D. Uram, K. Ke, A.J. Hunt, M. Mayer, Submicrometer pore-based characterization and quantification of antibody-virus interactions, Small. 2 (2006) 967–972. https://doi.org/10.1002/smll.200600006.
[129] H. Michelle Grandin, O. Guillaume-Gentil, T. Zambelli, M. Mayer, J. Houghtaling, C.G. Palivan, M. Textor, F. Höök, Bioinspired, nanoscale approaches in contemporary bioanalytics (Review), Biointerphases. 13 (2018) 040801. https://doi.org/10.1116/1.5037582.
[130] J.R. Lakowicz, Principles of Fluorescence Spectroscopy, Third Edit, Springer US, Boston, MA, 2006. https://doi.org/10.1007/978-0-387-46312-4.
[131] D. Evanko, A. Heinrichs, C.K. Rosenthal, Milestones in light microscopy, Nat. Cell Biol. 11 (2009) 1165–1165. https://doi.org/10.1038/ncb1009-1165.
[132] A. Jablonski, Efficiency of Anti-Stokes Fluorescence in Dyes, Nature. 131 (1933) 839–840. https://doi.org/10.1038/131839b0.

[133] R.I. MacDonald, Characteristics of self-quenching of the fluorescence of lipid-conjugated rhodamine in membranes, J. Biol. Chem. 265 (1990) 13533–13539.
[134] M. Minsky, Microscopy Apparatus, US Pat. 3013467. (1957). https://patents.google.com/patent/US3013467A/en.
[135] M. Minsky, Memoir on inventing the confocal scanning microscope, Scanning. 10 (1988) 128–138. https://doi.org/10.1002/sca.4950100403.
[136] S.W. Hell, J. Wichmann, Breaking the diffraction resolution limit by stimulated emission: stimulated-emission-depletion fluorescence microscopy, Opt. Lett. 19 (1994) 780. https://doi.org/10.1364/OL.19.000780.
[137] D. Axelrod, Cell-substrate contacts illuminated by total internal reflection fluorescence, J. Cell Biol. 89 (1981) 141–145. https://doi.org/10.1083/jcb.89.1.141.
[138] D. Axelrod, Total Internal Reflection Fluorescence, Annu. Rev. Biophys. Biomol. Struct. 13 (1984) 247–268. https://doi.org/10.1146/annurev.biophys.13.1.247.
[139] C. Gell, M. Berndt, J. Enderlein, S. Diez, TIRF microscopy evanescent field calibration using tilted fluorescent microtubules, J. Microsc. 234 (2009) 38–46. https://doi.org/10.1111/j.1365-2818.2009.03147.x.
[140] M.G. Honig, R.I. Hume, Fluorescent carbocyanine dyes allow living neurons of identified origin to be studied in long-term cultures, J. Cell Biol. 103 (1986) 171–187. https://doi.org/10.1083/jcb.103.1.171.
[141] M.G. Honig, R.I. Hume, Dil and DiO: versatile fluorescent dyes for neuronal labelling and pathway tracing, Trends Neurosci. 12 (1989) 333–341. https://doi.org/10.1016/0166-2236(89)90040-4.
[142] R. Peters, J. Peters, K.H. Tews, W. Bähr, A microfluorimetric study of translational diffusion in erythrocyte membranes, Biochim. Biophys. Acta - Biomembr. 367 (1974) 282–294. https://doi.org/10.1016/0005-2736(74)90085-6.
[143] G.M. Whitesides, The origins and the future of microfluidics., Nature. 442 (2006) 368–73. https://doi.org/10.1038/nature05058.
[144] Y. Xia, G. Whitesides, Soft lithography, Annu. Rev. Mater. Sci. 28 (1998) 153–184. https://doi.org/10.1146/annurev.matsci.28.1.153.
[145] A. Ainla, G.D.M. Jeffries, R. Brune, O. Orwar, A. Jesorka, A multifunctional pipette., Lab Chip. 12 (2012) 1255–61. https://doi.org/10.1039/c2lc20906c.
[146] A. Einstein, Über die von der molekularkinetischen Theorie der Wärme geforderte Bewegung von in ruhenden Flüssigkeiten suspendierten Teilchen, Ann. Phys. 322 (1905) 549–560. https://doi.org/10.1002/andp.19053220806.
[147] H. Qian, M.P. Sheetz, E.L. Elson, Single particle tracking. Analysis of diffusion and flow in two-dimensional systems, Biophys. J. 60 (1991) 910–921. https://doi.org/10.1016/S0006-3495(91)82125-7.
[148] J.C. Crocker, D.G. Grier, Methods of Digital Video Microscopy for Colloidal Studies, J. Colloid Interface Sci. 179 (1996) 298–310. https://doi.org/10.1006/jcis.1996.0217.
[149] G.E. Uhlenbeck, L.S. Ornstein, On the Theory of the Brownian Motion, Phys. Rev. 36 (1930) 823–841. https://doi.org/10.1103/PhysRev.36.823.
[150] X. Bian, C. Kim, G.E. Karniadakis, 111 years of Brownian motion, Soft Matter. 12 (2016) 6331–6346. https://doi.org/10.1039/C6SM01153E.
[151] X. Michalet, Mean square displacement analysis of single-particle trajectories with localization error: Brownian motion in an isotropic medium, Phys. Rev. E. 82 (2010) 041914. https://doi.org/10.1103/PhysRevE.82.041914.
[152] C. Haiden, T. Wopelka, M. Jech, F. Keplinger, M.J. Vellekoop, Sizing of Metallic Nanoparticles Confined to a Microfluidic Film Applying Dark-Field Particle Tracking, Langmuir. 30 (2014) 9607–9615. https://doi.org/10.1021/la5016675.
[153] W. Sutherland, LXXV. A dynamical theory of diffusion for non-electrolytes and the

molecular mass of albumin, London, Edinburgh, Dublin Philos. Mag. J. Sci. 9 (1905) 781–785. https://doi.org/10.1080/14786440509463331.
[154] M. von Smoluchowski, Zur kinetischen Theorie der Brownschen Molekularbewegung und der Suspensionen, Ann. Phys. 326 (1906) 756–780. https://doi.org/10.1002/andp.19063261405.
[155] G.G. Stokes, On the effect of the internal friction of fluids on the motion of pendulums, Pitt Press Cambridge, 1851.
[156] V. Filipe, A. Hawe, W. Jiskoot, Critical evaluation of nanoparticle tracking analysis (NTA) by NanoSight for the measurement of nanoparticles and protein aggregates, Pharm. Res. 27 (2010) 796–810. https://doi.org/10.1007/s11095-010-0073-2.
[157] D.T. Yang, X. Lu, Y. Fan, R.M. Murphy, Evaluation of nanoparticle tracking for characterization of fibrillar protein aggregates, AIChE J. 60 (2014) 1236–1244. https://doi.org/10.1002/aic.14349.
[158] P. Jönsson, J.P. Beech, J.O. Tegenfeldt, F. Höök, Shear-Driven Motion of Supported Lipid Bilayers in Microfluidic Channels, J. Am. Chem. Soc. 131 (2009) 5294–5297. https://doi.org/10.1021/ja809987b.
[159] R. Kubo, The fluctuation-dissipation theorem, Reports Prog. Phys. 29 (1966) 306. https://doi.org/10.1088/0034-4885/29/1/306.
[160] M.A. Day, The no-slip condition of fluid dynamics, Erkenntnis. 33 (1990) 285–296. https://doi.org/10.1007/BF00717588.
[161] A.J. Goldman, R.G. Cox, H. Brenner, Slow viscous motion of a sphere parallel to a plane wall—II Couette flow, Chem. Eng. Sci. 22 (1967) 653–660. https://doi.org/10.1016/0009-2509(67)80048-4.
[162] M.E. O'Neill, A sphere in contact with a plane wall in a slow linear shear flow, Chem. Eng. Sci. 23 (1968) 1293–1298. https://doi.org/10.1016/0009-2509(68)89039-6.
[163] M. Chaoui, F. Feuillebois, Creeping flow around a sphere in a shear flow close to a wall, Q. J. Mech. Appl. Math. 56 (2003) 381–410. https://doi.org/10.1093/qjmam/56.3.381.
[164] E. Bonaccurso, M. Kappl, H.-J. Butt, Hydrodynamic Force Measurements: Boundary Slip of Water on Hydrophilic Surfaces and Electrokinetic Effects, Phys. Rev. Lett. 88 (2002) 076103. https://doi.org/10.1103/PhysRevLett.88.076103.
[165] C.-H. Choi, K.J.A. Westin, K.S. Breuer, Apparent slip flows in hydrophilic and hydrophobic microchannels, Phys. Fluids. 15 (2003) 2897. https://doi.org/10.1063/1.1605425.
[166] B. Cross, A. Steinberger, C. Cottin-Bizonne, J.-P. Rieu, E. Charlaix, Boundary flow of water on supported phospholipid films, Europhys. Lett. 73 (2006) 390–395. https://doi.org/10.1209/epl/i2005-10416-4.
[167] E. Lauga, M. Brenner, H. Stone, Microfluidics: The No-Slip Boundary Condition, in: C. Tropea, A.L. Yarin, J.F. Foss (Eds.), Springer Handb. Exp. Fluid Mech., Springer Berlin Heidelberg, Berlin, Heidelberg, 2007: pp. 1219–1240. https://doi.org/10.1007/978-3-540-30299-5_19.
[168] T. Olsson, V.P. Zhdanov, F. Höök, Total internal reflection fluorescence microscopy for determination of size of individual immobilized vesicles: Theory and experiment, J. Appl. Phys. 118 (2015) 064702. https://doi.org/10.1063/1.4928083.
[169] S. Block, V.P. Zhdanov, F. Höök, Quantification of Multivalent Interactions by Tracking Single Biological Nanoparticle Mobility on a Lipid Membrane, Nano Lett. 16 (2016) 4382–4390. https://doi.org/10.1021/acs.nanolett.6b01511.
[170] V.P. Zhdanov, C.A. Keller, K. Glasmästar, B. Kasemo, Simulation of adsorption kinetics of lipid vesicles, J. Chem. Phys. 112 (2000) 900–909. https://doi.org/10.1063/1.480617.
[171] J. Andrecka, K.M. Spillane, J. Ortega-Arroyo, P. Kukura, Direct observation and control

of Supported lipid bilayer formation with interferometric scattering Microscopy, ACS Nano. 7 (2013) 10662–10670. https://doi.org/10.1021/nn403367c.
[172] K. Dimitrievski, Deformation of Adsorbed Lipid Vesicles as a Function of Vesicle Size, Langmuir. 26 (2010) 3008–3011. https://doi.org/10.1021/la904743d.
[173] H.-L. Wu, P. Chen, C. Chi, H.-K. Tsao, Y.-J. Sheng, Vesicle deposition on hydrophilic solid surfaces, Soft Matter. 9 (2013) 1908–1919. https://doi.org/10.1039/C2SM27450G.
[174] V.P. Zhdanov, Mechanism of rupture of single adsorbed vesicles, Chem. Phys. Lett. 641 (2015) 20–22. https://doi.org/10.1016/j.cplett.2015.10.053.
[175] D. Stroumpoulis, A. Parra, M. Tirrell, A kinetic study of vesicle fusion on silicon dioxide surfaces by ellipsometry, AIChE J. 52 (2006) 2931–2937. https://doi.org/10.1002/aic.10914.
[176] K.L. Weirich, J.N. Israelachvili, D.K. Fygenson, Bilayer Edges Catalyze Supported Lipid Bilayer Formation, Biophys. J. 98 (2010) 85–92. https://doi.org/10.1016/j.bpj.2009.09.050.
[177] P. Plunkett, B. a. Camley, K.L. Weirich, J.N. Israelachvili, P.J. Atzberger, Simulation of edge facilitated adsorption and critical concentration induced rupture of vesicles at a surface, Soft Matter. 9 (2013) 8420. https://doi.org/10.1039/c3sm50443c.
[178] B. Homayun, X. Lin, H.-J. Choi, Challenges and Recent Progress in Oral Drug Delivery Systems for Biopharmaceuticals, Pharmaceutics. 11 (2019) 129. https://doi.org/10.3390/pharmaceutics11030129.
[179] K.T. Savjani, A.K. Gajjar, J.K. Savjani, Drug Solubility: Importance and Enhancement Techniques, ISRN Pharm. 2012 (2012) 1–10. https://doi.org/10.5402/2012/195727.
[180] K.J. Frank, U. Westedt, K.M. Rosenblatt, P. Hölig, J. Rosenberg, M. Mägerlein, M. Brandl, G. Fricker, Impact of FaSSIF on the solubility and dissolution-/permeation rate of a poorly water-soluble compound, Eur. J. Pharm. Sci. 47 (2012) 16–20. https://doi.org/10.1016/j.ejps.2012.04.015.
[181] E. Barrow, A. V Nicola, J. Liu, Multiscale perspectives of virus entry via endocytosis, Virol. J. 10 (2013) 177. https://doi.org/10.1186/1743-422X-10-177.
[182] G.P.H. Dietz, M. Bähr, Delivery of bioactive molecules into the cell: the Trojan horse approach, Mol. Cell. Neurosci. 27 (2004) 85–131. https://doi.org/10.1016/j.mcn.2004.03.005.
[183] T. Tian, Y. Wang, H. Wang, Z. Zhu, Z. Xiao, Visualizing of the cellular uptake and intracellular trafficking of exosomes by live-cell microscopy, J. Cell. Biochem. 111 (2010) 488–496. https://doi.org/10.1002/jcb.22733.
[184] A. Suetsugu, K. Honma, S. Saji, H. Moriwaki, T. Ochiya, R.M. Hoffman, Imaging exosome transfer from breast cancer cells to stroma at metastatic sites in orthotopic nude-mouse models, Adv. Drug Deliv. Rev. 65 (2013) 383–390. https://doi.org/10.1016/j.addr.2012.08.007.
[185] C. GRANGE, M. TAPPARO, S. BRUNO, D. CHATTERJEE, P.J. QUESENBERRY, C. TETTA, G. CAMUSSI, Biodistribution of mesenchymal stem cell-derived extracellular vesicles in a model of acute kidney injury monitored by optical imaging, Int. J. Mol. Med. 33 (2014) 1055–1063. https://doi.org/10.3892/ijmm.2014.1663.
[186] O.P.B. Wiklander, J.Z. Nordin, A. O'Loughlin, Y. Gustafsson, G. Corso, I. Mäger, P. Vader, Y. Lee, H. Sork, Y. Seow, et al., Extracellular vesicle in vivo biodistribution is determined by cell source, route of administration and targeting, J. Extracell. Vesicles. 4 (2015) 26316. https://doi.org/10.3402/jev.v4.26316.
[187] M.A. Oberli, A.M. Reichmuth, J.R. Dorkin, M.J. Mitchell, O.S. Fenton, A. Jaklenec, D.G. Anderson, R. Langer, D. Blankschtein, Lipid Nanoparticle Assisted mRNA Delivery for Potent Cancer Immunotherapy, Nano Lett. 17 (2017) 1326–1335. https://doi.org/10.1021/acs.nanolett.6b03329.

[188] O.M. Szklarczyk, N. González-Segredo, P. Kukura, A. Oppenheim, D. Choquet, V. Sandoghdar, A. Helenius, I.F. Sbalzarini, H. Ewers, Receptor Concentration and Diffusivity Control Multivalent Binding of Sv40 to Membrane Bilayers, PLoS Comput. Biol. 9 (2013) e1003310. https://doi.org/10.1371/journal.pcbi.1003310.
[189] C. Yoshina-Ishii, Y.-H.M. Chan, J.M. Johnson, L.A. Kung, P. Lenz, S.G. Boxer, Diffusive Dynamics of Vesicles Tethered to a Fluid Supported Bilayer by Single-Particle Tracking, Langmuir. 22 (2006) 5682–5689. https://doi.org/10.1021/la0534219.
[190] C. Beyer, D.S. Pisetsky, The role of microparticles in the pathogenesis of rheumatic diseases, Nat. Rev. Rheumatol. 6 (2010) 21–29. https://doi.org/10.1038/nrrheum.2009.229.
[191] D.L.M. Rupert, C. Lässer, M. Eldh, S. Block, V.P. Zhdanov, J.O. Lotvall, M. Bally, F. Höök, Determination of Exosome Concentration in Solution Using Surface Plasmon Resonance Spectroscopy, Anal. Chem. 86 (2014) 5929–5936. https://doi.org/10.1021/ac500931f.
[192] H. Matsuda, Zur theorie der stationären strom-spannunos-kurven von redox-elektrodenreaktionen in hydrodynamischer voltammetrie, J. Electroanal. Chem. Interfacial Electrochem. 15 (1967) 325–336. https://doi.org/10.1016/0022-0728(67)85042-3.
[193] S. Sjoelander, C. Urbaniczky, Integrated fluid handling system for biomolecular interaction analysis, Anal. Chem. 63 (1991) 2338–2345. https://doi.org/10.1021/ac00020a025.
[194] R. Karlsson, H. Roos, L. Fägerstam, B. Persson, Kinetic and Concentration Analysis Using BIA Technology, Methods. 6 (1994) 99–110. https://doi.org/10.1006/meth.1994.1013.
[195] L. Sercombe, T. Veerati, F. Moheimani, S.Y. Wu, A.K. Sood, S. Hua, Advances and Challenges of Liposome Assisted Drug Delivery, Front. Pharmacol. 6 (2015) 1–13. https://doi.org/10.3389/fphar.2015.00286.
[196] K.B. Johnsen, J.M. Gudbergsson, M.N. Skov, L. Pilgaard, T. Moos, M. Duroux, A comprehensive overview of exosomes as drug delivery vehicles - Endogenous nanocarriers for targeted cancer therapy, Biochim. Biophys. Acta - Rev. Cancer. 1846 (2014) 75–87. https://doi.org/10.1016/j.bbcan.2014.04.005.
[197] X. Luan, K. Sansanaphongpricha, I. Myers, H. Chen, H. Yuan, D. Sun, Engineering exosomes as refined biological nanoplatforms for drug delivery, Acta Pharmacol. Sin. 38 (2017) 754–763. https://doi.org/10.1038/aps.2017.12.
[198] J. Liu, A. Stace-Naughton, X. Jiang, C.J. Brinker, Porous Nanoparticle Supported Lipid Bilayers (Protocells) as Delivery Vehicles, J. Am. Chem. Soc. 131 (2009) 1354–1355. https://doi.org/10.1021/ja808018y.
[199] J.M. Chan, L. Zhang, K.P. Yuet, G. Liao, J.-W. Rhee, R. Langer, O.C. Farokhzad, PLGA–lecithin–PEG core–shell nanoparticles for controlled drug delivery, Biomaterials. 30 (2009) 1627–1634. https://doi.org/10.1016/j.biomaterials.2008.12.013.
[200] C.B. Brooke, Biological activities of "noninfectious" influenza A virus particles, Future Virol. 9 (2014) 41–51. https://doi.org/10.2217/fvl.13.118.
[201] C.S. Heilingloh, A. Krawczyk, Role of L-Particles during Herpes Simplex Virus Infection, Front. Microbiol. 8 (2017) 1–7. https://doi.org/10.3389/fmicb.2017.02565.
[202] P.J. Klasse, Molecular determinants of the ratio of inert to infectious virus particles, 1st ed., Elsevier Inc., 2015. https://doi.org/10.1016/bs.pmbts.2014.10.012.
[203] P. Kukura, H. Ewers, C. Müller, A. Renn, A. Helenius, V. Sandoghdar, High-speed nanoscopic tracking of the position and orientation of a single virus, Nat. Methods. 6 (2009) 923–927. https://doi.org/10.1038/nmeth.1395.
[204] G. Young, N. Hundt, D. Cole, A. Fineberg, J. Andrecka, A. Tyler, A. Olerinyova, A.

Ansari, E.G. Marklund, M.P. Collier, et al., Quantitative mass imaging of single biological macromolecules, Science (80-.). 360 (2018) 423–427. https://doi.org/10.1126/science.aar5839.
[205] P.G. Spear, Herpes simplex virus: receptors and ligands for cell entry, Cell. Microbiol. 6 (2004) 401–410. https://doi.org/10.1111/j.1462-5822.2004.00389.x.
[206] D. Shukla, P.G. Spear, Herpesviruses and heparan sulfate: an intimate relationship in aid of viral entry, J. Clin. Invest. 108 (2001) 503–510. https://doi.org/10.1172/JCI200113799.
[207] P. Dechadilok, W.M. Deen, Hindrance Factors for Diffusion and Convection in Pores, Ind. Eng. Chem. Res. 45 (2006) 6953–6959. https://doi.org/10.1021/ie051387n.
[208] Q. Lubart, L. Sune, S. Block, S. Jõemetsa, E. Olsén, S. Kesarimangalam, F. Höök, M. Bally, E.K. Esbjörner, F. Westerlund, High Throughput Size-Determination and Multiplexed Fluorescence Analysis of Single Biological Particles in a Nanofluidic Device, (n.d.) in writing.